

**Potential periodic signals in blazars: significance, forecasting and deep learning**M. A. HASHAD,<sup>1,2</sup> A. HAMMAD,<sup>3</sup> AND AMR A. EL-ZANT<sup>2</sup><sup>1</sup>*Department of Basic Science, Modern Academy for Engineering and Technology, Elmokattam 11439, Egypt*<sup>2</sup>*Centre for Theoretical Physics, The British University in Egypt, Sherouk City, 11837, Cairo, Egypt*<sup>3</sup>*Theory Center, IPNS, KEK, 1-1 Oho, Tsukuba, Ibaraki 305-0801, Japan.*

## ABSTRACT

Blazars exhibit variable emission on diverse timescales. Some light curves show signs of quasiperiodic oscillations (QPOs), which may encode clues regarding the physical processes behind the emission or point to supermassive binary black holes. We analyzed five blazars with previously reported high significance year-long QPOs, applying the Lomb-Scargle periodogram and Weighted Wavelet Z-transform methods to *Fermi*-LAT data up to early 2025. We furthermore examined an additional source (PKS 0139-09), where nascent QPO may be present. As the light curves showed longer term trends, we detrended the data using an STL decomposition, which often revealed a large seasonal component. We find that detrending generally leads to an increase in the strength of the QPO signal. However, except for PG 1553+113, where a clearly persistent QPO signal is present, we detect transience on a timescale of  $\lesssim 4000$  days. We then forecast the light curves over the following four years, using a traditional statistical method as well as a Transformer-based deep learning model. Applied to a test set, the latter showed significant success in predicting behavior that seems unexpected from simple inspection of the past data. Analyzing the extended time series suggests a markedly weaker QPO signals over the coming years in cases where the transient behavior appears near the end of the observational data. In contrast, in the nascent candidate QPO source (PKS 0139-09) the signal is expected to strengthen significantly. These predictions, which may reflect the physical origin of the QPOs, can be tested against future data.

*Keywords:* Active galactic nuclei (16); Blazars (164); Non-thermal radiation sources (1119); High energy astrophysics (739); Supermassive black holes (1663); Time series analysis (1916); Periodic search; Deep learning forecasting

Corresponding author: M. A. Hashad  
Mohamed.Hashad@bue.edu.eg

hamed@post.kek.jp

Amr.Elzant@bue.edu.eg

---

Contents

1. Introduction	2
2. <i>Fermi</i> -LAT light curves	4
3. Search for Gamma-ray periodicity in the original light curves	6
3.1. Lomb–Scargle periodogram	6
3.1.1. Method	6
3.1.2. Application to the light curves	7
3.2. Weighted Wavelet Z-transform	8
4. Light curve decomposition and detrending	10
4.1. Method	10
4.2. Results of the detrending procedure	11
4.3. Possible quasiperiodic signals in the detrended light curves	12
5. Light Curve Forecasting	14
5.1. Motivation and general framework	15
5.2. Statistical learning forecasting: STLForecaster	15
5.3. Deep Learning forecasting: Transformers	15
5.3.1. Motivation and overview	15
5.3.2. The Attention Mechanism	17
5.3.3. Network structure	18
5.3.4. Training	19
5.3.5. Forecast and predictions	20
6. Conclusion	22

---

## 1. INTRODUCTION

Blazars are a prominent type of active galactic nuclei where an accreting supermassive black hole launches a relativistic jet aimed toward the observer (Ulrich et al. 1997; Blandford et al. 2019). The prevailing view holds that emission at X-ray and gamma-ray energies arises through inverse Compton scattering, with jet electrons boosting photons to high energies by scattering them. The required seed soft photons in the jet plasma may originate from ambient synchrotron photons (Madejski & Sikora 2016). Based on optical emission line features, blazars are classified into two subclasses: flat spectrum radio quasars (FSRQs), showing strong emission lines; and BL Lac objects, showing absent or weak emission lines (Urry & Padovani 1995).

A defining feature of blazars is their variable emission across the entire electromagnetic spectrum on diverse timescales, ranging from minutes to years (Rieger 2019; Urry 2011; Bhatta & Dhital 2020; Abhir et al. 2021; Abdollahi et al. 2024). Relatively recently, a growing number of studies have also identified potential quasiperiodic oscillations (QPOs) in the light curves (LCs) of some blazars (Ackermann et al. 2015; Prokhorov & Moraghan 2017; Tavani et al. 2018; Peñil et al. 2020; Agarwal et al. 2021; Hashad et al. 2023; Peñil et al. 2024; Abdollahi et al. 2024; Hashad et al. 2024; Rico et al. 2025). This is of potential significance, as the existence of QPOs may harbor implications regarding the nature of quasar engines, their jets and their emission mechanisms (Mohan & Mangalam 2015; Benkhali et al. 2020). Importantly, they may furthermore be relevant as probes of supermassive black hole binary (SMBHB) systems (Begelman et al. 1980; Agazie et al. 2023; D’Orazio & Charisi 2023; Kiehlmann et al. 2025a; de la Parra et al. 2025), where orbital motions may cause jet precessions (e.g., Sobacchi et al. 2017), perturbation by magneto-gravitational stress (e.g., Cavaliere et al. 2017), or perturbations in the accretion flow (e.g., Doğan et al. 2015; Farris et al. 2014). This is a possibility that comes with important implications for contemporary cosmology, where the repeated hierarchical merging of dark matter halos—with the galaxies they embed and the supermassive black holes in their centers—is a definite prediction (Begelman et al. 1980; Volonteri et al. 2003; Maiolino et al. 2024). Indeed, the enumeration of potential SMBHB systems, from observations as well as through cosmological simulations, is currently an active area of research (Krause et al. 2025; Pfeifle et al. 2025; Puerto-Sánchez et al. 2025), and the field is further driven by upcoming gravitational wave experiments like LISA (Colpi et al. 2024).

Observed QPO signals in blazar LCs may be of the order of a month or shorter and up to the scale of years. On the shorter end, clear transience in the signals tends to be present. Such trends may be plausibly associated with ballistic motion in the blazar jet, such as in the curved helical blob model (Sarkar et al. 2021; Sharma et al. 2024; Tantry et al. 2025; Peñil et al. 2025a). In this case, the helical motion of a plasma blob generates periodic variations in the flux, and the curvature of the jet results in a variable viewing angle (and hence the apparent decay in QPO amplitudes).

For candidate QPOs potentially originating from SMBHB systems, the simplest assumption is to associate the QPO periods with the orbital timescale of a bound binary system undergoing gravitational wave (GW) ringdown. A simple geometric interpretation of QPO in terms of jet precession in an SMBHB system predicts a QPO timescale of the order of years lest the ringdown becomes too rapid for the signal to have a realistic chance of being observed (Sobacchi et al. 2017). In some models, where orbital motion causes helical (but non-ballistic) motion in the jet, the observed QPO timescale is expected to be shortened by at least an order of magnitude, due to light travel time effects (in proportion to the square of the bulk Lorentz factor; Rieger 2004). But in such cases, the allowed intrinsic orbital period may also be much larger (in a purely geometric model, the maximum timescale is limited by the observable precession angle). Thus, any potentially observable QPO signal due to an SMBHB would be expected to appear on the longest timescale. Such signals can be detected with any confidence, which for  $\gamma$ -ray data is of the order of years.

Confirming or ruling out QPOs with year-long periods presents particular difficulties, given that the total observing time in the  $\gamma$ -ray regime is not far longer than the purported periodic timescale (Peñil et al. 2025b; Peñil et al. 2025; for recent studies of longer term data at other wavelengths see, e.g. Kiehlmann et al. 2025b; Molina et al. 2025). This is especially the case if the signals are accompanied by longer term trends, including longer term periodicities or transience in the signal. Detecting transience, in particular, may also be important in distinguishing between possible physical origins of apparent QPO signals. For example, in purely geometric SMBHB models, there is no obvious mechanism to damp the QPO signals over observable timescales.

To test for the persistence of the QPO one may also make predictions by extending LCs based on past behavior, which can be compared with future observations. An increase in the significance of the QPO signal reflects a strong quasi-stationary signal. A decrease, on the other hand, may point to the presence of transience. The results of the predictions encode patterns that can be used to detect and predict non-stationarity in the process underlying the signal. Such predictions can be made using traditional statistical forecasting methods (Rico et al. 2025), or through the rapidly developing machine learning techniques. In the present study, we use examples of both.

Recent advances in deep learning (DL) have provided powerful alternatives to traditional statistical forecasting techniques for analyzing complex time series. Classical statistical models, such as autoregressive or decomposition-based methods, typically assume linearity, stationarity or fixed periodicities, which limit their ability to capture the nonlinear, multi-scale variability and noise contamination that characterize astrophysical data. In contrast, DL approaches learn hierarchical feature representations directly from the data, enabling them to model nonlinear correlations and

disentangle long- and short-term trends. This makes DL particularly advantageous for forecasting the highly variable emission of gamma-ray blazars, where primary emission processes span diverse physical timescales and are further modulated by jet and environmental effects. Among DL techniques, Transformers are particularly well suited for the task at hand, given their ability to capture both local variability and global periodic trends, and are more adaptable to irregularly sampled or incomplete time series, a common challenge in astrophysical observations. Unlike other related methods, it does not suffer from shortcomings such as vanishing or exploding gradients, difficulties in learning very long sequences, and sequential processing that hinders parallelization. Transformers overcome these shortcomings through their attention mechanism, which directly models relationships between all time steps without relying on recurrence. They can thus make relatively reliable predictions regarding the existence and persistence (or otherwise) of QPO signals, which may furthermore be tested against future observations.

Toward these goals, we re-analyze five blazars previously reported to show strong QPO signals. We use *Fermi*-LAT LCs extended up to February 2025. We also examine the blazar PKS 0139-09, which shows a possible long-period QPO along with a strong upward trend in its LC. As such trends constitute a significant complication in quantifying the significance of possible QPO signals of a shorter period, we remove them by de-trending the data. We then forecast the LCs four years into the future, testing the predictions on a test set and re-analyzing the extended light curves obtained *via* the Transformer method.

The paper is organized as follows. Section 2 describes the *Fermi*-LAT Gamma-ray data. Gamma-ray QPOs in the observed LCs are analyzed in Section 3. Decomposition and detrending of the LCs is presented in Section 4. In Section 5, we introduce the statistical method (STLForecaster) and a deep learning (Transformer) approach for forecasting the LCs and present the results. We discuss and summarize our findings in Section 6.

## 2. FERMI-LAT LIGHT CURVES

Aboard the Fermi satellite, the Fermi Large Area Telescope (*Fermi*-LAT) is a pair-conversion gamma-ray detector sensitive from  $\sim 20$  MeV to 500 GeV. Since the start of its operating mode in August 2008, *Fermi*-LAT has continuously scanned the full-sky every two orbits (at  $\approx 1.6$  hr per orbital period) with its wide ( $\approx 2.4$  sr) field of view. This provides long-coverage observations across diverse timescales, extending from hours to years. The LAT also has superior angular resolution (point spread function, PSF  $< 0.8^\circ$ ) and the largest effective area ( $\sim 8000$  cm<sup>2</sup>) at photon energy above 1 GeV (Atwood et al. 2009).

This work uses LAT observations of six blazars, covering  $\approx 16.5$  years in the energy range 100 MeV–300 GeV. Five of the sources were selected because they have been previously reported in the literature to exhibit  $\gamma$ -ray QPOs with high significances (e.g., Zhang et al. 2017; Bhatta & Dhital 2020; Wang et al. 2022; Abdollahi et al. 2024; Peñil et al. 2024; Peñil et al. 2025). These are: PG 1553+113, PKS 0454-234, PKS 2155-304, OJ 014, and S5 1044+71, see Table 1. With the aim of testing for long term non-stationarity and transience, we extend their study using monthly binned LCs up to February 2025. The LCs were generated using the maximum likelihood technique utilizing `fermipy`<sup>1</sup>, a Python package for standard `ScienceTools` implementation (Version 1.2.2; Wood et al. 2017). To further test for non-stationary behavior, we do the same for a novel candidate QPO source (PKS 0139-09), where we suspect nascent oscillations to be starting within the observed period.

To select the photons composing the LCs, the Pass 8 ‘SOURCE’ class (EVENT\_CLASS = 128) was used from the instrument response function `P8R3_SOURCE_V3`, as well as event type “FRONT+BACK” (EVENT\_TYPE = 3) (Atwood et al. 2013). Regions of interest (ROI) of  $15^\circ \times 15^\circ$  square, centered at the source, were chosen to account for photons within it. A zenith angle cut ( $> 90^\circ$ ) was applied to eliminate  $\gamma$ -ray contamination from the Earth’s limb. Standard data quality selections (DATA\_QUAL  $> 0$ ) && (LAT\_CONFIG == 1) were also implemented, and time intervals overlapping with LAT-detected  $\gamma$ -ray bursts and solar flares were excluded. Sources from the 4FGL catalog (Abdollahi et al. 2022) were modeled using the standard LAT analysis. They were positioned within  $20^\circ$  from center of the ROI and incorporating the Galactic (`gll_iem_v07.fits`) and isotropic diffuse emissions (`iso_P8R3_SOURCE_V3_v1.txt`).

The maximum likelihood analysis was conducted over the entire period of observation, from August 2008 to February 2025. We used eight logarithmic energy bins per decade and  $0.1^\circ$  spatial bins. Sources in the ROI were modeled with their spectral shapes and parameters values set from the catalog. The normalization and spectral index of the

<sup>1</sup> <http://fermipy.readthedocs.io>

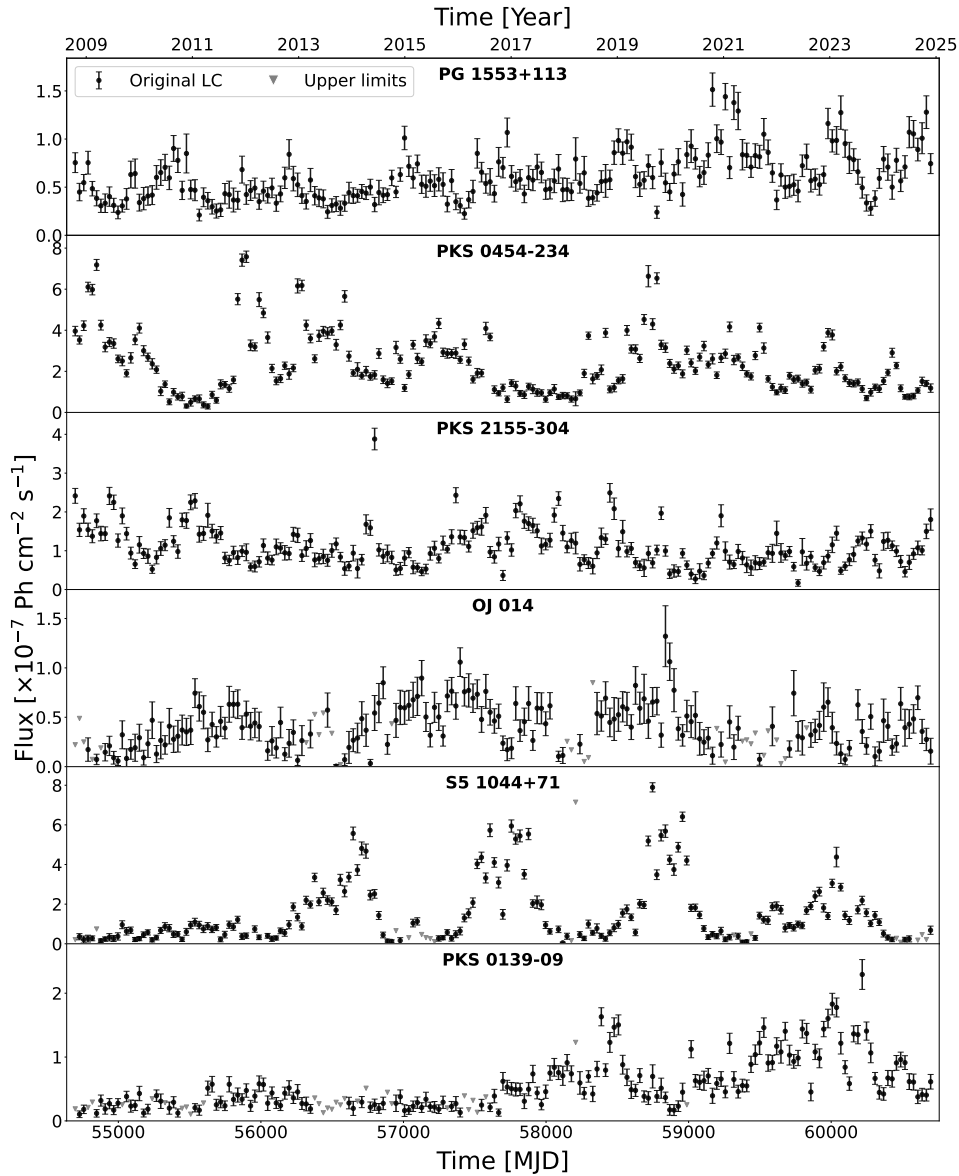


**Figure 1.** Extended *Fermi*-LAT  $\gamma$ -ray integrated flux light curves of the selected blazars. The five previously reported with high-significance periodicity, and the new QPO candidate, PKS 0139-09. The light curves span  $\approx 16.5$  yr, from August 2008 to February 2025. The down gray triangles are for bins with upper limits, where their Test Statistic values  $< 9$  ( $\approx 3\sigma$ ).

target source, as well as the normalization of the sources within a  $3^\circ$  radius from the target position and both diffuse backgrounds, were left free to vary. A good fit quality was obtained (`fit_quality = 3`) by iteratively running the routines `gta.optimize()` and `gta.fit()`.

In order to generate the LC of each source, we binned the data into one month bins. Each bin was then subjected to a full likelihood fit, using the parameters' values attained from the main stream analysis on the entire LC. During the fit the following parameters converge to their best fit values: the target's spectral parameters, the normalizations of sources within  $3^\circ$  from the center of the ROI, and the normalizations of the diffuse components. The temporal bins with Test Statistic values (TS)  $< 9$  ( $\approx 3\sigma$ ) were set as upper limits. TS determines the source detection significance (TS =  $-2\log(L_0/L_1)$ ), where  $L_0$  and  $L_1$  are the likelihood functions evaluated at the best-fit model parameters without and with the target source, respectively. The resulting  $\gamma$ -ray LCs of the six sources are shown in Fig. 1.

**Table 1.** Our blazar sample, given by their association name in the point sources *Fermi*-LAT fourth catalog (4FGL). We list the equatorial coordinates (deg), type, redshift, and  $\gamma$ -ray QPOs' periods in literature and their significances. The types of AGN: BL Lacertae (bll) and flat-spectrum radio quasar (fsrq). Examples of periods previously reported in the literature. All refer to analysis of  $\gamma$ -ray data from *Fermi*-LAT, with the significances obtained through the LSP method.

Source Name	4FGL Name	RA (J2000)	Dec (J2000)	Type	$z$	Reported Period (yr)	Observation Period	Ref.
PG 1553+113	J1555.7+1111	238.931	11.188	bll	0.433	$2.1^{+0.2}_{-4.0\sigma}$	2008-08–2023-11	1
						$2.1^{+0.2}_{-5.1\sigma}$	2008-08–2020-12	2
PKS 0454–234	J0457.0-2324	74.261	-23.415	fsrq	1.003	$3.6^{+0.2}_{-3.2\sigma}$	2008-08–2020-12	2
PKS 2155–304	J2158.8-3013	329.714	-30.225	bll	0.116	$1.7^{+0.1}_{-4.9\sigma}$	2008-08–2016-10	3
						$1.7^{+0.1}_{-4.1\sigma}$	2008-08–2020-12	2
OJ 014	J0811.4+0146	122.861	1.776	bll	1.148	$4.2^{+0.5}_{-3.2\sigma}$	2008-08–2020-12	2
S5 1044+71	J1048.4+7143	162.107	71.730	fsrq	1.150	$3.1^{+0.4}_{-3.6\sigma}$	2012-03–2021-03	4
PKS 0139–09	J0141.4-0928	25.363	-9.483	bll	0.733	--	--	--

**References.** (1) (Abdollahi et al. 2024) (2) (Peñil et al. 2025) (3) (Zhang et al. 2017) (4) (Wang et al. 2022).

### 3. SEARCH FOR GAMMA-RAY PERIODICITY IN THE ORIGINAL LIGHT CURVES

We investigated the  $\approx 16.5$ -yr LCs, as obtained above, using the Lomb-Scargle periodogram (LSP) and Weighted Wavelet Z-transform (WWZ), as we describe below.

#### 3.1. Lomb–Scargle periodogram

##### 3.1.1. Method

The LSP is a widely used algorithm for identifying periodicity in unevenly sampled astronomical time-series (Lomb 1976; Scargle 1982). The standard normalized Lomb-Scargle periodogram is equivalent to fitting sinusoidal functions of the form,  $y(t) = A\cos(\omega t) + B\sin(\omega t)$  to an LC. It is defined, for time series  $(t_i, y_i)$ , as

$$P(\omega) = \frac{1}{2} \left\{ \frac{(\sum_i y_i \cos(t_i - \tau))^2}{\sum_i \cos^2(t_i - \tau)} + \frac{(\sum_i y_i \sin(t_i - \tau))^2}{\sum_i \sin^2(t_i - \tau)} \right\},$$

where

$$= \frac{1}{2\omega} \tan^{-1} \left( \frac{\sum_i \sin(2\omega t_i)}{\sum_i \cos(2\omega t_i)} \right). \quad (1)$$

To a first approximation, the power spectral density (PSD) of blazars LCs may be characterized by a simple power-law (PL) in the form of  $P(\nu) \propto \nu^{-\beta}$ , where  $\nu$  is the temporal frequency and  $\beta$  is the power spectral slope or PL index, signifying that blazar variability is a colored noise-like process (Goyal et al. 2017; Bhatta & Dhital 2020). The observed characteristic slope range is approximately 1-3, across time-scales from minutes up to decades (e.g., flicker/pink noise for  $\beta \sim 1$  and red noise for  $\beta \sim 2$ ), which differs from the flatter ( $\beta \sim 0$ ) PSD signifying uncorrelated white noise (Press 1978).

The presence of periodicity is then searched for by identifying additional peaks superposed on the power law. The period uncertainty is then estimated from the half-width at half-maximum of a Gaussian function fitted to the profile at the position of the peak.

As blazars LCs are noisy, and can have irregular sampling or contain gaps (Benkhali et al. 2020; Tarnopolski et al. 2020; Goyal et al. 2017; Goyal 2018), spurious peaks could arise and caution is warranted (Vaughan et al. 2016; VanderPlas 2018). To account for this, we employed simulated LCs from using the Emmanoulopoulos et al. (2013) approach to estimate the significance of the peaks found from the data. These LCs are statistically equivalent to the original LC in terms of the PSD, probability density function, and data sampling.

**Table 2.** Summary of Lomb-Scargle periodogram periods with their significance for the original  $\gamma$ -ray light curves of the six blazars. The PKS 0139-09 blazar has two periods.

PG 1553+113	PKS 0454–234	PKS 2155–304	OJ 014	S5 1044+71	PKS 0139–09
$2.1^{+0.13}_{3.6\sigma}$	$3.5^{+0.35}_{2.5\sigma}$	$1.7^{+0.13}_{2.6\sigma}$	$4.2^{+0.57}_{3.5\sigma}$	$3.1^{+0.34}_{4.4\sigma}$	$5.2^{+0.73}_{1.6\sigma}$

We used  $10^6$  simulated LCs utilizing the implementation from Connolly (2015). Each simulated LC was subjected to the LSP, where a specified confidence level is then the percentile at each period in the frequency grid. It should be noted that, given the number of the simulated LCs, the maximum significance achievable is  $\approx 4.8\sigma$ .

### 3.1.2. Application to the light curves

The results of the LSP applied to the observed LCs of the six blazars are summarized in Table 2. Below we discuss their significance in light of previous work.

The BL Lac object PG 1553+113 is a remarkable case that showed almost sinusoidal modulation in its LC in the first 7 yr of *Fermi*-LAT data (Ackermann et al. 2015); with a period of  $2.18 \pm 0.08$  yr, covering about three oscillation cycles and chance probability of being spurious of  $< 1\%$ . These initial findings have been supported by several follow-up studies, in  $\gamma$ -ray as well as optical wavelengths through extended datasets and more analyses (e.g., Sobacchi et al. 2017; Tavani et al. 2018; Benkhali et al. 2020; Ren et al. 2023; Peñil et al. 2024; Chen et al. 2024; Abdollahi et al. 2024). Recently Abdollahi et al. (2024) have used 15 yr of *Fermi*-LAT data—doubling the observation time of the first claim—to confirm the 2.1 yr-PG 1553+113  $\gamma$ -ray QPO. By extending the *Fermi*-LAT data to February 2025, and using a monthly binned LC, we find QPO in PG 1553+113 of 2.1 yr period by using LSP at  $3.6\sigma$ . This is consistent with their results for the original LC (by LSP;  $3.5\sigma$ ). After detrending their LC their reported significance increased to  $4\sigma$ . As we will see below (Section 4), we also obtain a larger significance ( $4.5\sigma$ ) after detrending.

In our analysis, the FSRQ PKS 0454-234 showed a QPO with period of  $3.5 \pm 0.35$  yr at  $2.5\sigma$ . This period has been previously reported at the higher significance of  $3.2\sigma$  by Peñil et al. (2025) and by Rico et al. (2025) at the still higher  $4.8\sigma$ , both using about 12 yr of the LAT data and using LSP. Peñil et al. (2025) reported also similar periods at significances of  $2.8\sigma$ ,  $2.4\sigma$ , and  $2.8\sigma$  using the methods, Generalized Lomb–Scargle periodogram (GLSP; Zechmeister & Kürster 2009), Phase dispersion minimization (PDM; Stellingwerf 1978), and Continuous Wavelet Transform (CWT; Torrence & Compo 1998), respectively. We also identify possible signals with smaller periods. Remarkably, like the previously reported principal peak, which turns out to have a nearby larger period peak, they tend to come in pairs. Some are consistent with being harmonic at half, a third, and a tenth of the previously reported period, as will be seen below in connection to Fig. 2. As we will also see, these secondary peaks are actually detected through the LSP with higher significance than the primary (although they are of smaller height, they correspond to more cycles). High frequency secondary peaks are present in other cases, though only for the present source and the nascent QPO candidate (PKS 0139-09) do they come with higher significance than the principal period.

The BL Lac object PKS 2155-304 has been reported by Zhang et al. (2017), using data from August 2008 to October 2016, to display a significant (by LSP;  $4.9\sigma$ )  $\gamma$ -ray QPO with period  $1.7 \pm 0.13$  yr. This finding is consistent with the results of Sandrinelli et al. (2014). Similar period using LSP has been reported in the optical and  $\gamma$ -ray using almost 10 years of data by Chevalier et al. (2019), as well as in the X-ray, UV, and optical bands by Peñil et al. (2024). Using almost the first ten years of *Fermi*-LAT data, Benkhali et al. (2020) reported the same period (1.7 yr) from GLSP at  $3.7\sigma$ . The significance of the period decreased to  $4.1\sigma$  (by LSP) and  $3.3\sigma$  (by GLS and CWT) during the  $\gamma$ -ray observation period from August 2008 to December 2020 (Peñil et al. 2025). Using the decade-long *Fermi*-LAT data, Bhatta & Dhital (2020) found two quasi-periodic features for this object in both LSP and WWZ methods, one at 1.7 yr and the other at 0.7 yr both at significance of  $\gtrsim 99.99\%$ . Moreover, their WWZ analysis showed that over the year, the low-frequency period is gradually shifting toward a slightly higher frequency. PKS 2155-304 has been identified as a low-significance  $\gamma$ -ray QPO candidate (August 2008–April 2021) with period of  $0.91 \pm 0.29$  yr at  $2.2\sigma$  using CWT, where it exhibited a time-dependent behavior, with decreasing frequency in time (Ren et al. 2023). By extending the observation period to the beginning of 2025 in this study, the period significance from LSP decreased to  $2.6\sigma$ . As we

will see, this decrease is partly due to long term trends and transience; due to low-frequency modulation and to the principal QPO signal itself diminishing with time.

The BL Lac object OJ 014 was reported to exhibit a  $\gamma$ -ray QPO with period of about 4.2 yr during the period from August 2008 to December 2020 at significance of  $3.2\sigma$  (by LSP),  $2.6\sigma$  (by GLSP and PDM), and  $3.6\sigma$  (by CWT) (Peñil et al. 2025). The auto-correlation function for twelve years of *Fermi*-LAT data showed a period of  $4.0 \pm 0.3$  yr at  $2\sigma$  (Peñil et al. 2024). In this study, the LSP for the LC of this object revealed a period of  $4.2 \pm 0.57$  yr with a small increase in the period’s significance to  $3.5\sigma$ .

The FSRQ object S5 1044+71 was reported with QPO of period  $3.1 \pm 0.4$  yr in its  $\gamma$ -ray LC using LSP during the period from March 2012 to March 2021 at  $3.6\sigma$  (Wang et al. 2022), and also during the period from August 2008 to December 2020 at  $4.8\sigma$  (Rico et al. 2025). The same period from the CWT was identified by Ren et al. (2023) at significance of  $4.9\sigma$  using  $\gamma$ -ray data from August 2008 to April 2021. We confirm the consistency of the QPO in the  $\gamma$ -ray LC with a potential period of  $3.1 \pm 0.34$  yr (by LSP) at  $4.4\sigma$ .

The BL Lac object PKS 0139-09 was not previously reported as a source of QPO. It has been included in this work as it seems an ideal test case for the purpose of studying and forecasting non-stationary behavior in QPO. As of now, the LSP for this object revealed two peaks in the PKS 0139-09  $\gamma$ -ray LC with two tentative candidate periods at  $0.67 \pm 0.04$  yr and  $5.2 \pm 0.73$  yr, with significances of  $2.2\sigma$  and  $1.6\sigma$ , respectively. Although the larger period is of weaker significance, if this is due to the lack of hitherto observed cycles it should be expected to significantly strengthen in the future. We thus consider this to be the principal period despite its relatively small significance (again it seems possible to associate the smaller period, detected with higher significance, with a high order harmonic; of order  $\sim 8$ ).

In summary, examining possible QPO signals in LCs studied over different timespans considered here generally leads to similar periods as previously reported but with different significances. In addition, we clearly detect secondary peaks, which in some cases come with higher significance than the primary peaks and are not inconsistent with being harmonics. In general, the significances of the previously reported periodicities (associated with the primary peak) do not necessarily increase with the increased timespan considered here. They generally stay approximately the same or significantly decrease with the increased time interval. This can be either due to the principal QPO signal itself being transient, or because the signal includes superposed low-frequency modes that come with large red noise. We explore these possibilities below.

### 3.2. Weighted Wavelet Z-transform

To examine the effect of transients we use the WWZ wavelet technique. While the LSP excels at periodicity detection in unevenly sampled LCs, it cannot optimally accommodate QPOs exhibiting significant frequency or amplitude evolution over time. For such phenomena the WWZ proves more effective for detection and quantification. The WWZ is based on a concept analogous to the LSP, but with an important difference; it still fits sinusoidal waves to the data, but with wave localization in both the time and frequency domains (e.g., Foster 1996). As the computation of WWZ is demanding, we used only 20,000 simulated LCs, which corresponds to a maximum significance of  $3.9\sigma$ . For sources with periods estimated with significances exceeding the  $3.9\sigma$  level, such as PG 1553+113, OJ 014, and S5 1044+71, the number of simulated LCs was increased to  $10^6$  to boost the maximum significance to  $\approx 4.8\sigma$ .

In Fig. 2, we show the 2D contour plots of the WWZ power for the blazar LCs considered. The major higher significance peaks, associated with the brightly shaded strips, correspond to the periods previously inferred using the LSP. The principal periods obtained through the two methods are consistent within uncertainties, and with broadly similar significances. However, the WWZ diagrams show non-trivial temporal structures.

Notable non-stationary features may be spotted in the WWZ map of PKS 2155-304. This shows a transient pattern with three epochal periods, with the period decreasing by a factor of about  $3/5$  times from one epoch to the next. The first epoch, lasting  $\approx 9$  years, has a significant period of 1.7 yr (at  $2.9\sigma$ ); this is followed by a period of 1.0 yr ( $2\sigma$ ) in the second epoch; and 0.56 yr ( $2\sigma$ ) in the third. With the LSP we find an additional significant period at  $0.35 \pm 0.003$  yr at  $2.2\sigma$ —again consistent with being  $3/5$  times the period at 0.56 (which is confirmed at  $0.56 \pm 0.006$  yr and  $2.3\sigma$ )—repeating the aforementioned pattern.

A more stable but still palpably time dependent pattern may also be inferred for PKS 0454-234. Here we note even more significant peaks associated with higher frequencies. Like the double peak at the main period, these also come in

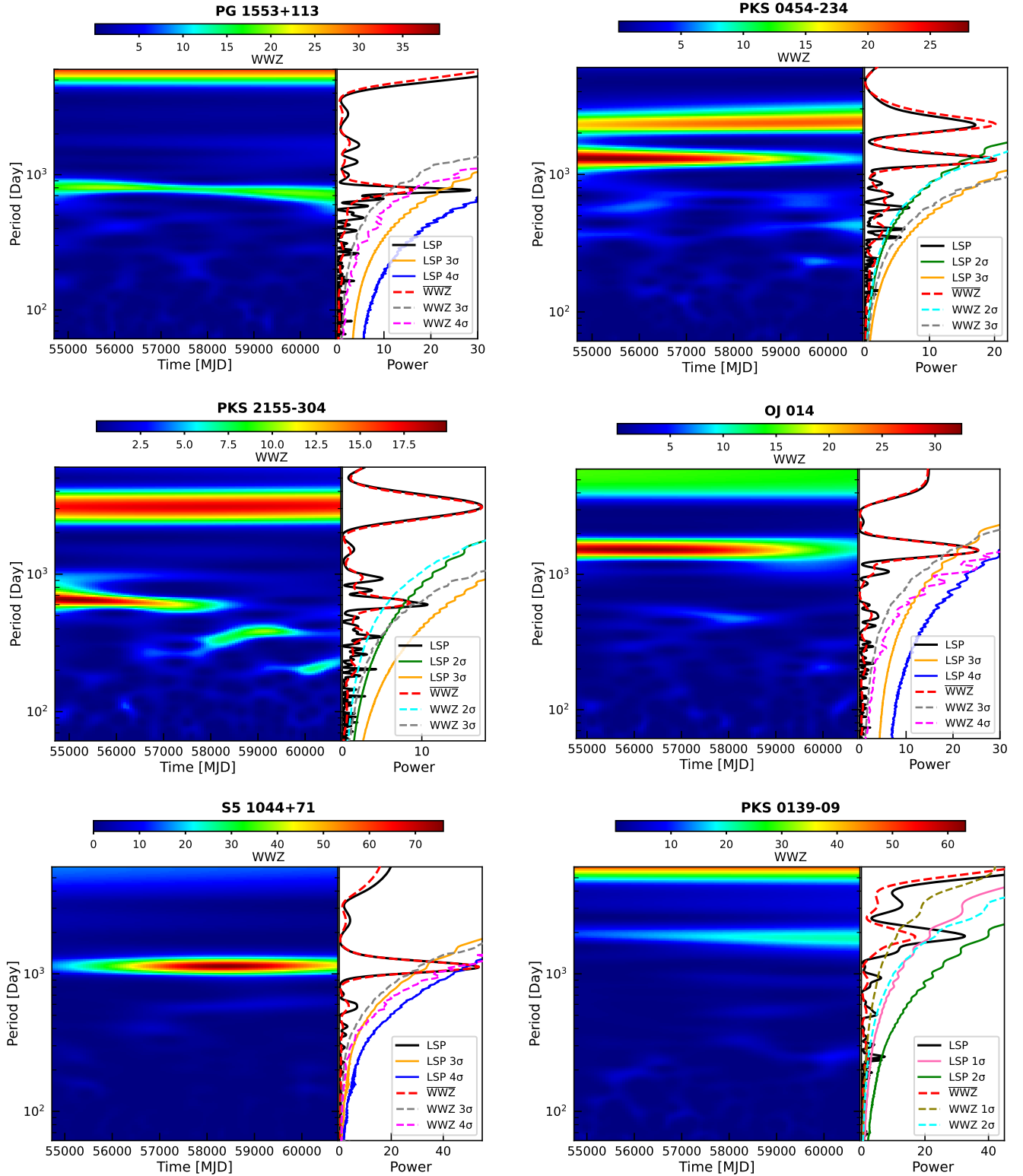


**Figure 2.** The 2D scalogram-filled color scale contour plots of the Weighted Wavelet Z-transform for the  $\gamma$ -ray light curves of the selected sample. Side plots are the corresponding WWZ power spectrum averaged (red dashed line) and the LSP power spectrum (black line), scaled to the WWZ peak. The pink, green, orange, and blue lines denote the  $1\sigma$ ,  $2\sigma$ ,  $3\sigma$ , and  $4\sigma$  LSP's confidence levels, respectively. The olive, cyan, gray, and magenta dashed lines represent the corresponding WWZ confidence levels using the Emmanoulopoulos et al. (2013) method.

pairs, and some may correspond to harmonics. They are particularly clear in the LSP analysis. For example, there is a peak at  $1.57 \pm 0.05$  yr, detected with the LSP at  $2.1\sigma$  significance, which is consistent with being half the principal period at  $3.5 \pm 0.35$  yr; another peak at  $1.1 \pm 0.02$  yr, with significance  $2.6\sigma$ , is consistent with being a third of the principal peak period; and another at  $0.37 \pm 0.003$  yr, detected with significance  $2.6\sigma$ , with period consistent with being a tenth of the main one. We note that the last two periods have slightly higher significance than the principal peak (at  $2.5\sigma$ ). Even higher significance comes with the peaks for 0.96 and 0.39 years ( $2.7\sigma$  and  $3\sigma$ , respectively), which are 'twinned' with two of the secondary peaks above (at 1.1 and 0.37 years).

We note that significant higher frequency peaks are also present in the case of PG 1553+113. Here they appear, according to the LSP analysis, at  $0.45 \pm 0.005$  and  $0.71 \pm 0.01$  years (the latter being clearly consistent with having a period of a third of the main one). But they are of small significance relative to the main period at  $2.1 \pm 0.1$  yr, detected at  $3.9\sigma$ . In contrast to what was found above, in the case of PG 1553+113 the strength of the periodic signal is consistent over the whole time-range considered.

The diagram for S5 1044+71 also exhibits a single clearly defined peak at  $3.1 \pm 0.31$  yr, with no other reaching a significance of  $2\sigma$ . But, unlike with PG 1553+113, it is time dependent. The corresponding WWZ strip peaks in brightness within the second half of the time interval considered here; it corresponds to the high significance of  $4.6\sigma$ . Though high, this is somewhat smaller than that reported by Ren et al. (2023), who found a period of  $3.1 \pm 0.62$  at  $> 5\sigma$ . This may be due to the transient behavior already apparent in the brightening and fading of our strip in the panel corresponding to that source in Fig. 2.

Only in the case of PG 1553+113 do we detect a persistent QPO over the whole observed timescale. Otherwise, either the signal fades well within the observational timespan of the data considered here (PKS 0454-234, PKS 2155-304), or near its end (OJ 014, S5 1044+71); or, (in the case of PKS 0139-09) the apparent QPO are nascent and expected to intensify if present. These distinctive traits will be important when discussing the predicted future light curves (Section 5.3.5).

While smaller periods are detected in some of the cases, with some consistent with being harmonics, in most cases we furthermore find brightly shaded bands at lower frequencies (larger periods) than the principal peak (appearing at the top of the diagrams). These may be associated with longer term periodic or transient phenomena. The exceptions being S5 1044+71, where such a band is nearly absent, and PKS 0454-234 where the higher period band is just above the principal one. As we will see, such properties will determine the effect of the detrending procedure on the significance of the principal periods.

## 4. LIGHT CURVE DECOMPOSITION AND DETRENDING

### 4.1. Method

Simple inspection (of Fig. 3) reveals that some blazar LCs display long-term trends alongside possible periodic signals with relatively short periods. This is an effect that was also present in previous studies (e.g., Rueda et al. 2022; Abdollahi et al. 2024; Peñil et al. 2024; Rico et al. 2025). As trends distort the embedded periodic signals, they affect any inferred statistical significance regarding the presence of periodicity (Rueda et al. 2022). They may also reflect QPO modulation on longer timescales (with larger errors). The inclusion of such trends in the fit of a source's behavior may thus be essential in estimating the significance of any inferred periodicity on characteristic timescales shorter than the trend (Welsh 1999; Rico et al. 2025).

With this in mind, we decompose our LC time series into components that correspond to distinct temporal variations (Makridakis et al. 1998). Namely,

1. **A Trend Component:** reflecting low-frequency, or systematic long-term variation in the data amplitudes.
2. **A Seasonal Component:** capturing cyclical variation aligned with smaller periodic frequencies, such as daily, weekly, or annual patterns.
3. **A Remainder Component:** representing variation unaccounted for by trend or seasonality, which may contain noise or latent informational patterns.

Traditional decomposition frameworks often assume mutual independence among components, formalized by decomposing an observed time series  $Y_t$  with  $n$  data points through an additive model:

$$Y_t = T_t + S_t + R_t, \quad t = 1, \dots, n. \quad (2)$$

Here  $T_t$ ,  $S_t$ , and  $R_t$  denote the long-term trend, the seasonality, and the remainder (or irregularities), respectively. For this purpose, we used the STLForecaster<sup>2</sup>; a statistical model that employs a decomposition-based framework to generate predictions for both LC detrending and forecasting. Rooted in the principles of time series decomposition, this method applies the filtering procedure STL (Seasonal-Trend Decomposition via LOESS), introduced by Cleveland (1990), to decompose a given time series to the aforementioned components (trend, seasonal, and residual). The predicted time series is then derived by independently modeling each component. It is also possible to recombine their projections (as described in Section 5.2).

The STL algorithm iteratively applies LOESS (locally estimated scatterplot smoothing). This is a non-parametric local regression smoothing technique. It is used to isolate seasonal and trend-cycle patterns while accounting for local variations. Unlike rigid parametric models (e.g., the parametric model to search for periods in LCs of high-energy  $\gamma$ -ray sources, Rueda et al. 2022), the STL’s modular architecture comprises sequential smoothing iterations. It thus ensures robustness in handling diverse temporal structures, including nonlinear trends and evolving seasonality. It derives its strength from the ability to specify the number of observations per cycle of seasonal components; resilience to short-term anomalies or transient behavior in the data; and compatibility with time series including gaps (Cleveland 1990). This is needed, as our sample includes three sources with gaps in their LCs—OJ 014, S5 1044+71, and PKS 0139-09. One of these has many missing values, mostly during source’s low-states ( $\approx 16\%$ ). To overcome this issue, we interpolate its LC employing a linear interpolation method. This is further discussed in Section 5.2.

For each point  $x$  in the time series, LOESS implements a weighted regression on a selected nearest neighbor window. The weights of neighbors  $x_i$  follow a weighting function  $W$ , e.g., Gaussian or tri-cube function, where the weight decreases as with the distance  $x_i$  from  $x$ . The neighborhood weight for any  $x_i$  is then

$$\nu_i(x) = W \left( \frac{|x_i - x|}{\lambda(x)} \right), \quad (3)$$

where  $\lambda(x)$  is the distance amplitude from  $x$ .

The essential outputs of the procedure are the strengths of the trend and seasonality in the LCs (Wang et al. 2006). The trend strength is defined as Makridakis et al. (1998)

$$F_T = \max \left( 0, 1 - \frac{\text{Var}(R_t)}{\text{Var}(T_t + R_t)} \right), \quad (4)$$

where  $\text{Var}(T_t + R_t)$  and  $\text{Var}(R_t)$  are the variances of the deseasonalized series and the series after trend and seasonality adjusting, respectively. In time series exhibiting a strong trend, the seasonally adjusted series demonstrates significantly greater variability than the remainder. Consequently, the variance ratio  $\text{Var}(R_t)/\text{Var}(T_t + R_t)$  will be substantially reduced. Conversely, data with minimal or absent trend exhibit approximately equivalent variances between the remainder and the seasonally adjusted series. Similarly, the seasonality strength is defined by,

$$F_S = \max \left( 0, 1 - \frac{\text{Var}(R_t)}{\text{Var}(S_t + R_t)} \right), \quad (5)$$

where  $\text{Var}(S_t + R_t)$  is the variance of the detrended series. A series with strong seasonality gives  $F_S$  close to unity, as  $\text{Var}(S_t + R_t)$  will be much greater than  $\text{Var}(R_t)$ , while a series with almost no seasonality gives  $F_S$  close to zero. The remainder strength,  $F_R$ , is computed by replacing  $\text{Var}(R_t)$  in the previous equation by  $\text{Var}(S_t)$ .

#### 4.2. Results of the detrending procedure

Fig. 3 shows the decomposition of the monthly  $\gamma$ -ray LCs using the STL method. In the case of PG 1553+113 the procedure reveals a general increasing trend over time, followed by apparent oscillations. We note that in previous

<sup>2</sup> [https://www.sktime.net/en/stable/api\\_reference/auto\\_generated/sktime.forecasting.trend.STLForecaster.html](https://www.sktime.net/en/stable/api_reference/auto_generated/sktime.forecasting.trend.STLForecaster.html)

studies, the trend for this source was modeled as a linear increase during the first  $\approx 12$ -15 years of *Fermi*-LAT data (Abdollahi et al. 2024; Peñil et al. 2024; Rico et al. 2025). However, by extending the LC with currently available *Fermi*-LAT data up to February 2025, it is evident that the flux has followed a saturating path rather than continuing to monotonically increase. The STL method captures this reversal that was not accounted for in previous work. In other cases the trend appears to exhibit clear time modulation, particularly in the case of PKS 0454-234 (where we recall had a larger period peak close to the main one in its periodogram; Fig. 2).

In general, all blazars in the sample exhibited long-term trends, albeit with varying strength and timescales. These were captured in the contour plots of the WWZ, where they are represented as bands or peaks referring to tentative low-frequency signals (Fig. 2). In addition to significant trend components all sources exhibited seasonality values above 0.55, with the exception of PKS 2155-304. For this source, the strength of the seasonality fades after the first  $\approx 9$  years of observations, which is consistent with the transient behavior also inferred from the WWZ in Fig. 2. In contrast, in the case of S5 1044+71 the seasonal component increases with time, but it comes with a noisy residual that appears correlated with it over the first three peaks of the original LC and then anti-correlated with the fourth. We finally note the strong seasonal component for PKS 0454-234 despite the low significance level of the main period at 3.5 years. This further suggests that the smaller period peaks found in Fig. 2 may indeed be effectively harmonics that contribute towards a strong overall seasonal quasiperiodic (but non-sinusoidal) signal.

### 4.3. Possible quasiperiodic signals in the detrended light curves

We now repeat the LSP and WWZ analysis on the detrended LCs. As is immediately clear from Fig. 4, the detrending removes the low frequency signals previously found with low significance (compare with Fig. 2, where they are represented by the bands at the upper end of the panels). As may be expected, major differences in QPO signal significances are found when these are prominent.

The results are summarized in Table 3. The main periods identified for the detrended LCs are the same as, or within the uncertainties of, those from the original LCs. The statistical significances, on the other hand, increase significantly in all cases; with exceptions for PKS 0454-234, where the major band at lower frequency was previously found to be of similar period to the main QPO signal (Fig. 2), and the case of S5 1044+71, where a clear low frequency band is absent. In the latter case, although a significant trend is present, it seems to correspond to a more diffuse band of lower frequencies.

**Table 3.** Summary of the periods and their significances, as inferred from the data, for both original and detrended  $\gamma$ -ray light curves of the six blazars.

Source Name	Original LC		Detrended LC	
	LSP	WWZ	LSP	WWZ
PG 1553+113	$2.1^{+0.13}_{-3.6\sigma}$	$2.1^{+0.19}_{-3.9\sigma}$	$2.1^{+0.12}_{-4.5\sigma}$	$2.1^{+0.18}_{-4.0\sigma}$
PKS 0454-234	$3.5^{+0.35}_{-2.5\sigma}$	$3.5^{+0.42}_{-2.2\sigma}$	$3.6^{+0.4}_{-2.6\sigma}$	$3.6^{+0.44}_{-2.4\sigma}$
PKS 2155-304	$1.7^{+0.13}_{-2.6\sigma}$	$1.7^{+0.17}_{-2.9\sigma}$	$1.7^{+0.13}_{-3.3\sigma}$	$1.7^{+0.16}_{-3.3\sigma}$
OJ 014	$4.2^{+0.57}_{-3.5\sigma}$	$4.2^{+0.53}_{-3.6\sigma}$	$4.2^{+0.53}_{-4.2\sigma}$	$4.2^{+0.55}_{-4.3\sigma}$
S5 1044+71	$3.1^{+0.34}_{-4.4\sigma}$	$3.1^{+0.31}_{-4.6\sigma}$	$3.1^{+0.37}_{-4.3\sigma}$	$3.1^{+0.35}_{-4.4\sigma}$
PKS 0139-09	$5.2^{+0.73}_{-1.6\sigma}$	$5.1^{+0.71}_{-1.7\sigma}$	$5.1^{+0.96}_{-2.0\sigma}$	$5.0^{+0.80}_{-2.0\sigma}$

In general, the post-detrending increase in the strength of the QPO signal was larger in the case of the LSP-inferred periods than with the local in time WWZ method. But it was still not always large enough to account for the high significance levels in previous work, where the LCs were studied on a shorter time interval. This is notably the case with PKS 2155-304, which is also the case in which the transient nature of the QPO signal seems clearest. Thus, in addition to the contamination by slow time dependent modulation that may be removed by detrending, intrinsic transience in the signal strength at the principal period may affect the significance of the QPO signal at that period over time. Except for the case PG 1553+113, clear transience is present in the WWZ diagrams of the detrended data as was the case with the original LCs.

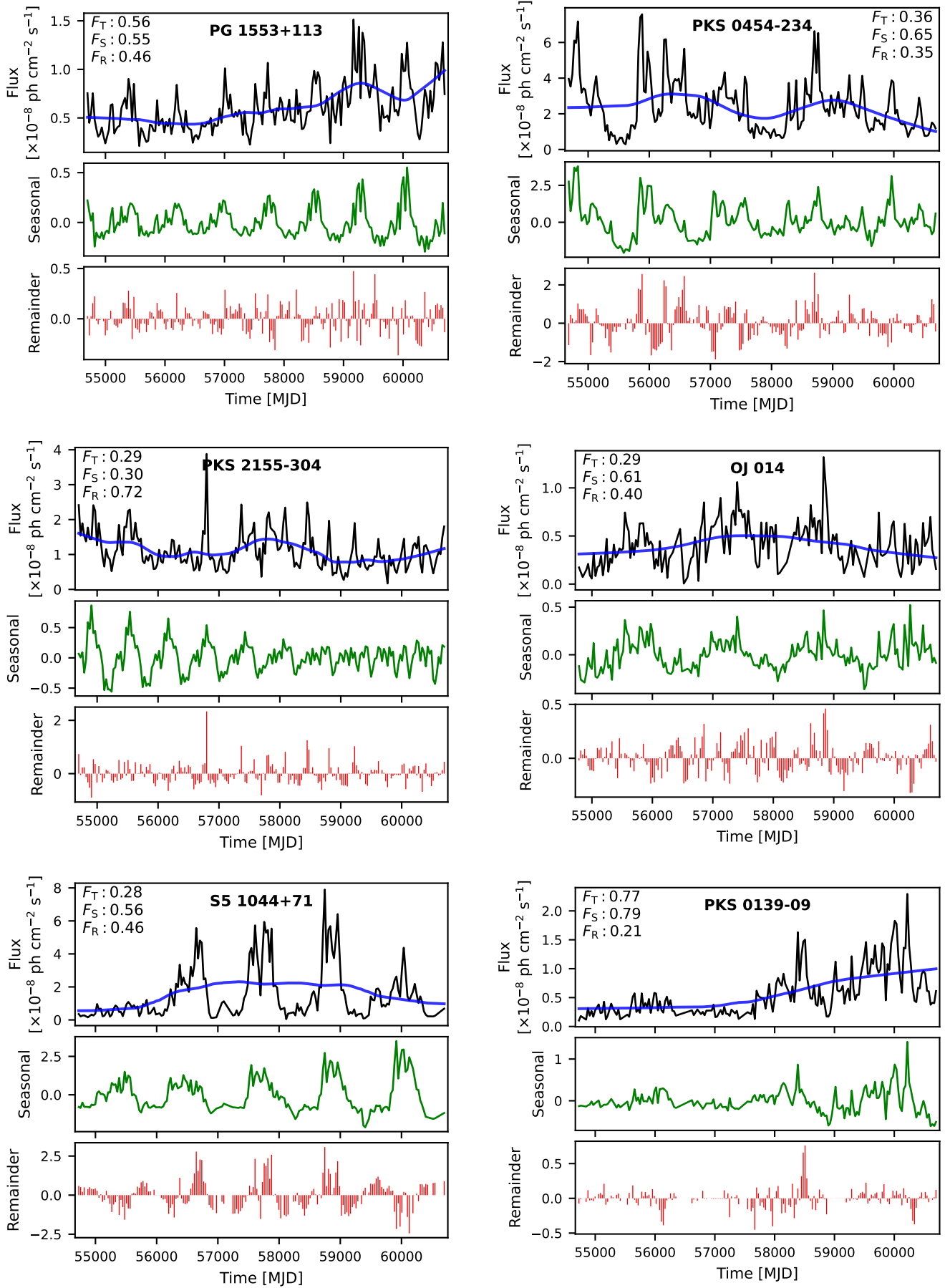


**Figure 3.** Decomposition of the monthly  $\gamma$ -ray light curves using the STL method. For each source, the trend (blue curve) component is depicted in the top panel with source's original light curve (black curve). The seasonal and remainder components are displayed in the middle and bottom panels, respectively. The strength of the components are as denoted in the panels.

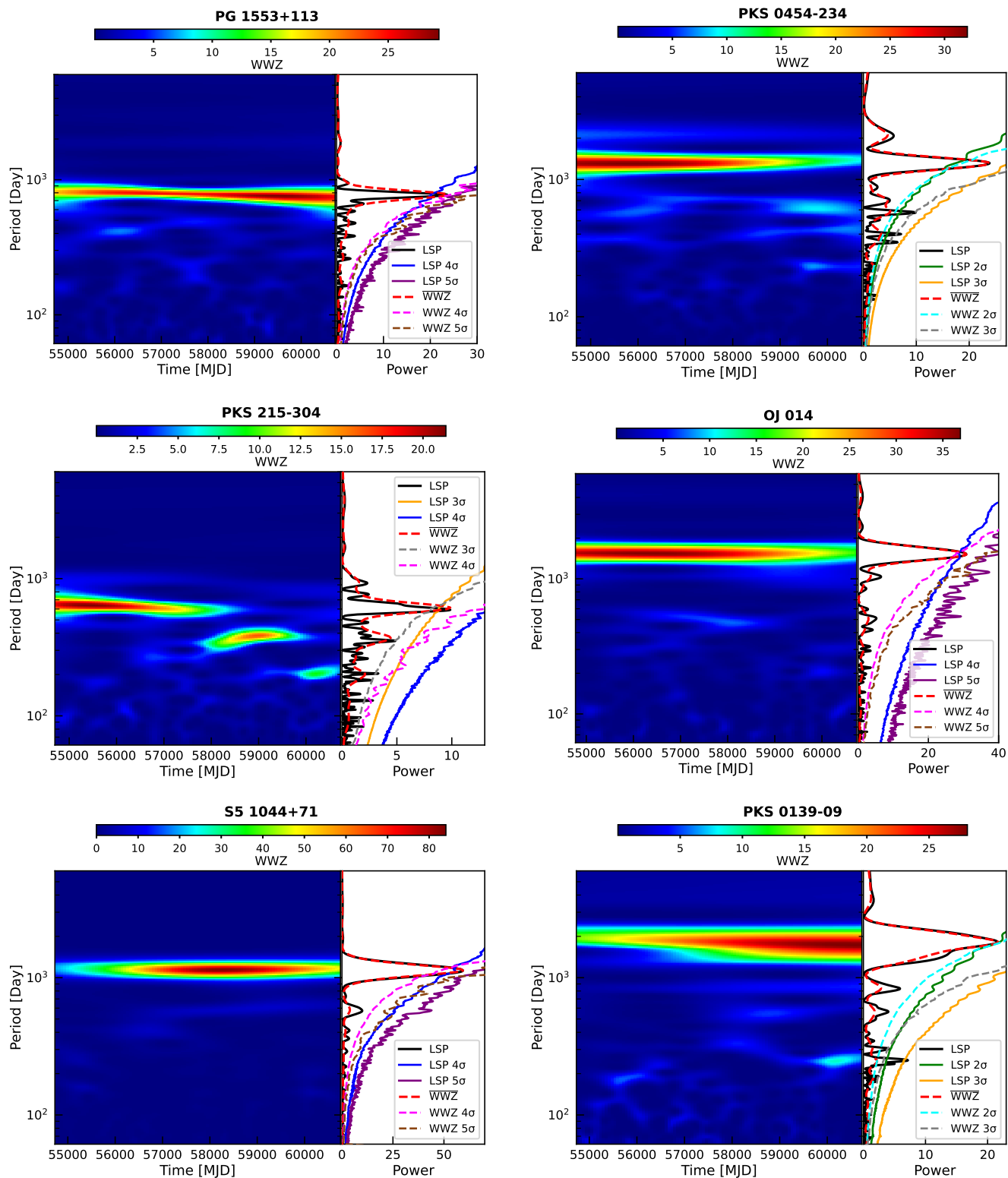


**Figure 4.** Same as Fig. 2 but for the detrended light curves. The  $5\sigma$  confidence levels for the Lomb-Scargle periodogram and the Weighted Wavelet Z-transform, from applying the Emmanoulopoulos et al. (2013) method, are presented by purple line and brown dashed line, respectively.

## 5. LIGHT CURVE FORECASTING

### 5.1. Motivation and general framework

Forecasting future signals is important in our context, as it enables to make testable predictions that may ascertain or rule out sustained QPO signals, which may contain important clues to their strength and physical origin. Persistence of QPOs in extrapolated curves reflect their strength of an existing QPO and makes testable predictions that may be compared with data from future observational campaigns.

For this purpose, we will use both the traditional statistical method of the previous section, in addition to a more recent machine learning based technique described below.

#### 5.2. Statistical learning forecasting: *STLForecaster*

So far we have used the detrending procedure in order to isolate a periodic signal from a general trend and residual of an existing time series. But the method is also commonly used for forecasting future signals. The associated *STLForecaster* framework enhances forecasting accuracy through the decomposition of the time series into its constituent components, as in the previous section. Forecasts are then generated by extrapolating the deterministic trend and seasonal cycles into future intervals and combining these projections with stochastic residual estimates. This component-wise approach ensures that systematic patterns and random fluctuations are modeled independently. This leads to improvement in overall predictive reliability.

The LC is split into training and test datasets, with the test set comprising approximately quarter of the complete observation period of the LC to evaluate the model's performance. To optimize the hyperparameters involved, we performed a grid search over predefined search spaces using the machine learning method `ForecastingGridSearchCV` (from `sktime.forecasting.model_selection`) with scoring metric mean squared error (MSE). The mean absolute percentage error (MAPE), which measures the deviation of predictions from the actual (ground-truth) observations, was also computed for the comparison with the Transformer (Sec. 5.3). The critical hyperparameter seasonal period `sp`, which defines the length of the seasonal period passed to `statsmodels` STL, is then assigned a range of values centered around the determined period. While autocorrelation and partial autocorrelation plots are standard statistical tools for analyzing time series and inferring periodic signals, the determined period was instead obtained by the robust periodicity analysis method employed. In this study, the LSP is used.

Another important hyperparameter is `forecaster_trend`. The trend component extracted via STL decomposition is fitted to a polynomial function to project future trend. For modeling the seasonal component, the `NaiveForecaster(strategy="last")` outperformed different tested forecasters. This aligns with the expectation that seasonal behavior often closely resembles its most recent period (Hyndman & Athanasopoulos 2021).

The residual of the future period is set to the mean of the residual component of the STL decomposition. The prediction is then the sum of the predictions of trend, seasonal, and residual components. The results of this procedure are presented in Fig. 5. They will be compared to those obtained by the Transformer technique described below.

### 5.3. Deep Learning forecasting: Transformers

#### 5.3.1. Motivation and overview

Compared to classical statistical approaches, such as those described in the preceding subsection (STL), Transformers offer clear advantages for Gamma-ray blazar forecasting. STL relies on additive decomposition into smooth seasonal, trend, and residual components, which makes it effective for regular, stationary time series but poorly suited for the highly irregular and non-stationary variability of blazars. In particular, STL assumes fixed periodicities and smooth variations, limiting its ability to model sudden flaring events or quasiperiodic oscillations. Moreover, while STL focuses on short-term extrapolation of trends, it cannot naturally account for long-range temporal dependencies or multi-scale variability.

Unlike traditional sequential models that propagate information step by step, the Transformer attends to all time steps simultaneously. This makes it especially suitable for forecasting (Wen et al. 2022; Shin & Zhang 2025). For forecasting, the Transformer first processes sequential flux measurements from the existing LCs. The temporal structure of these sequences contains both rapid short-term flaring activity and long-range quasiperiodic variability, and the attention mechanism allows the model to capture both simultaneously. This is critical when forecasting over a horizon of 48 time steps.

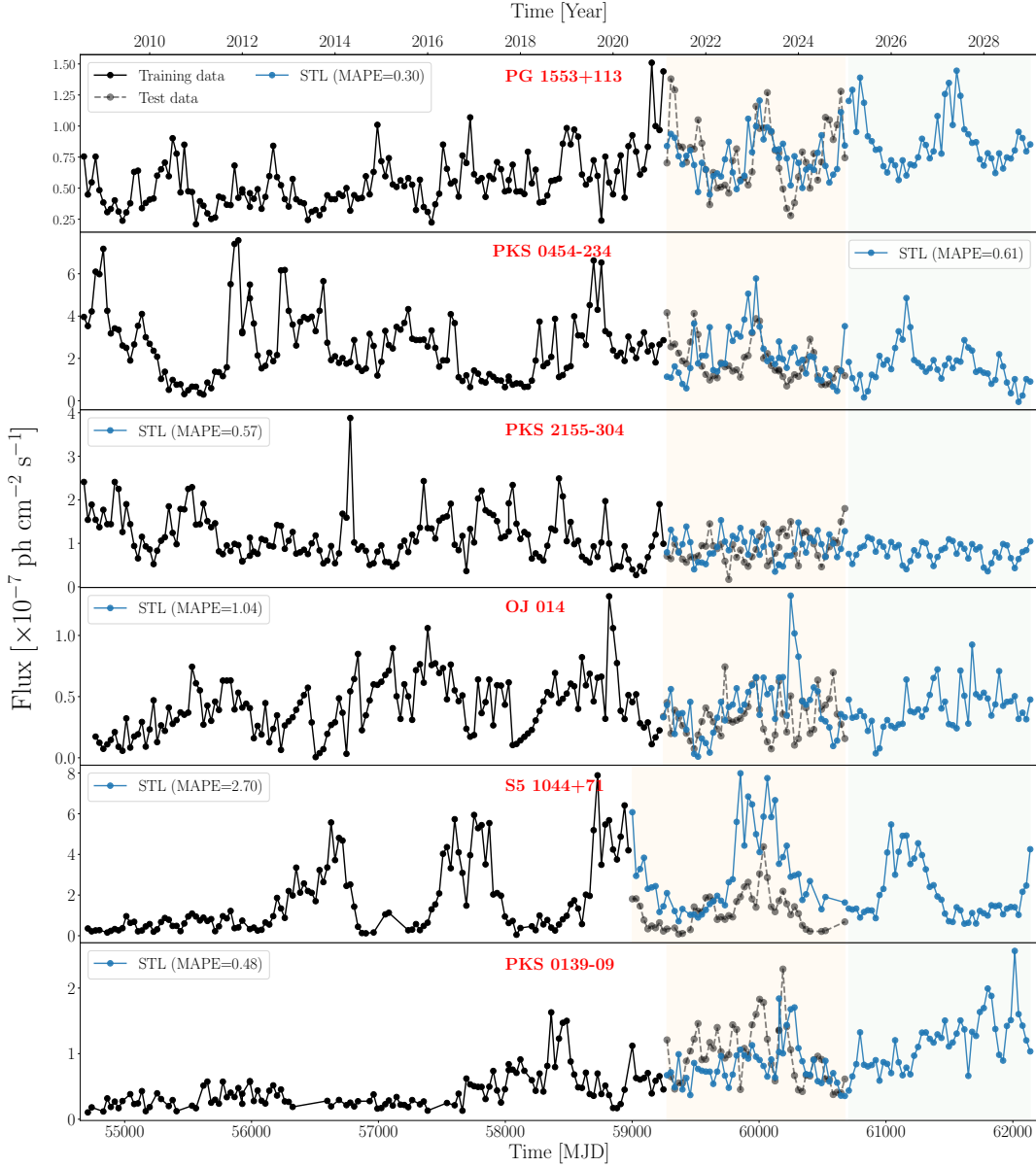


**Figure 5.** Current observed monthly  $\gamma$ -ray light curves and their forecast for the following four years. The blue line represents the light curve predictions on the test set (pink highlighted region) and the future epoch (light blue highlighted region) using STLForecaster. The Mean Absolute Percentage Error (MAPE) for the test set predictions is presented. The prediction on the future epoch is based on the training on the entire observed light curve.

At the core of Transformer architectures lies the *attention mechanism*, which computes weighted interactions among sequence elements. These weights reflect how strongly different time steps influence each other. This is learned adaptively through training.

The input to the Transformer is a tensor  $X \in \mathbb{R}^{T \times F}$ , where  $T$  denotes the number of observed past time steps and  $F$  the number of features per step. In the simplest case,  $F = 1$  corresponds to flux values alone; however, additional contextual variables (e.g., flux uncertainties, spectral indices, or external observational flags) may also be incorporated. Each input vector  $X_{t,*}$  is projected into a higher-dimensional latent space through an embedding layer, which enriches the representation and enables the network to capture nonlinear dynamics beyond the raw flux signal.

The model then generates outputs  $\hat{Y} \in \mathbb{R}^{H \times F}$ , where  $H = 48$  is the forecast horizon. Each predicted time step  $\hat{Y}_h$  corresponds to a forecasted flux value (or set of features)  $h$  steps ahead of the most recent observation. This direct

mapping from past context to future trajectory is what distinguishes Transformers from statistical decomposition-based approaches.

### 5.3.2. The Attention Mechanism

Self-attention in Transformers allows the model to capture dependencies across all time steps simultaneously, unlike traditional recurrent models that process data sequentially. This global view enables the network to identify long-term patterns and seasonal trends in time series data more effectively. Self-attention also provides dynamic weighting of past observations, so the model can focus on the most relevant historical points for each prediction. Furthermore, it is highly parallelizable, making training on large datasets faster and more efficient compared to sequential architectures. Overall, self-attention enhances the model's ability to handle complex, non-linear temporal relationships, improving the accuracy and robustness of forecasts.

The embedded sequence,  $X^{\text{embed}}$ , of length  $T$  is transformed into queries ( $Q$ ), keys ( $K$ ), and values ( $V$ ) by learnable linear projections (Vaswani et al. 2017)

$$Q^{T \times d} = X^{\text{embed}}W^Q, \quad K^{T \times d} = X^{\text{embed}}W^K, \quad V^{T \times d} = X^{\text{embed}}W^V, \quad (6)$$

where  $d$  is the latent dimensionality encoding the minimal effective number of degrees of freedom through which the data may be represented and  $W^Q$ ,  $W^K$ , and  $W^V$  are their learnable weight matrices.

Attention scores quantify the relative importance of different time steps in the input light curve when constructing the prediction at a given epoch. In this context, they measure how strongly past flux states influence the current forecast, enabling the model to dynamically focus on the most informative temporal patterns while down-weighting irrelevant or noisy observations. This adaptive weighting allows the network to capture both short- and long-range temporal correlations. The attention scores are computed as

$$\alpha^{T \times T} = \text{softmax} \left( \frac{QK^T}{\sqrt{d}} \right), \quad (7)$$

where  $\alpha_{ij}$  measures the contribution of time step  $j$  when updating step  $i$  and  $K^T$  denotes the transpose of the key matrix. In blazar LCs, this enables the model to focus on temporally distant but correlated variability, capturing flaring episodes and long-memory effects.

The aggregated output is:

$$\mathcal{Z} = \alpha V, \quad (8)$$

where  $\mathcal{Z}$  represents a context-aware reconstruction of the sequence. Multi-head attention extends this mechanism by learning multiple relational subspaces in parallel: some heads specialize in short-term fluctuations, while others capture broader, slowly evolving trends.

The outputs from all attention heads are concatenated and linearly projected back to the model's embedding dimension by the learned weight matrix  $W^O$ :

$$\mathcal{O} = \text{concat}(\mathcal{Z}^1, \dots, \mathcal{Z}^n)W^O, \quad (9)$$

and combined with the original embedding through a residual connection:

$$\tilde{X} = X^{\text{embed}} + \mathcal{O}, \quad (10)$$

which stabilizes training and preserves temporal structure. Stacking multiple Transformer blocks allows progressive refinement of temporal dependencies across scales.

The self-attention mechanism in Transformers directly captures both short- and long-term correlations within the LC, enabling the model to simultaneously learn rapid flux fluctuations and slowly evolving patterns. This makes it a powerful forecasting tool that adapts dynamically to the complexity of blazar variability, providing accurate predictions over horizons as large as 48 steps. As a result, the Transformer architecture provides a flexible, data-driven alternative to statistical decomposition methods. Its ability to learn multi-scale temporal dependencies and adapt to irregular variability makes it particularly well-suited for forecasting the complex and dynamic behavior of gamma-ray blazars.

### 5.3.3. Network structure

The forecasting network is constructed upon a Transformer encoder tailored to capture temporal dependencies in multivariate time series. Each input sequence consists of 96 past observations. Prior to embedding, the raw input series  $x_t$  is decomposed into two components, a slowly varying trend and a rapidly fluctuating residual, according to

$$x_t = T_t + R_t. \quad (11)$$

Here  $T_t$  denotes the trend component, representing smooth long-term variations;  $R_t$  denotes the residual, capturing short-term fluctuations, irregularities, and seasonal patterns. Importantly, the two components are processed independently:  $T_t$  and  $R_t$  are each passed through separate linear embedding layers and then through parallel stacks of Transformer encoders. In this way, each encoder is specialized in learning the temporal dependencies of either the long-term trend or the high-frequency residual. The resulting encoded representations are concatenated at the output of the encoder stage, providing the forecasting head with complementary information from both structural components of the time series. This decomposition and parallel encoding stabilize optimization by reducing interference between long- and short-range patterns, while also improving interpretability.

To preserve temporal ordering, positional encodings are added to the embeddings, as the self-attention mechanism is inherently permutation-invariant (Hammad et al. 2024; Hammad & Nojiri 2024). In this work, sinusoidal positional encodings are used, defined as

$$\text{PE}_{(pos,2i)} = \sin\left(\frac{pos}{10000^{2i/d_{\text{model}}}}\right), \quad \text{PE}_{(pos,2i+1)} = \cos\left(\frac{pos}{10000^{2i/d_{\text{model}}}}\right), \quad (12)$$

where  $pos$  is the position index,  $i$  indexes the embedding dimensions, and  $d_{\text{model}} = 256$  is the embedding size. Positional encoding introduces explicit information about the position of each element, allowing the model to distinguish values at different time steps and capture temporal dependencies. Without it, the Transformer would interpret the input as an unordered set, preventing effective learning of sequential patterns. Positional encoding is essential for Transformers in time series forecasting because self-attention is inherently permutation-invariant and does not encode the order of sequence elements. In time series, temporal order is critical, as the relative timing of observations carries important information for forecasting.

Each of the trend and residual encoder branches consists of four Transformer encoder layers. Each layer contains a multi-head self-attention mechanism with  $h = 8$  heads, followed by a position-wise feed-forward network. Given an input representation  $X \in \mathbb{R}^{L \times d_{\text{model}}}$ , queries  $Q$ , keys  $K$ , and values  $V$  are computed through learned linear projections. The scaled dot-product attention is then expressed as

$$\text{Attention}(Q, K, V) = \text{softmax}\left(\frac{QK^\top}{\sqrt{d_k}}\right) V, \quad (13)$$

where  $d_k = d_{\text{model}}/h$  is the dimension per head. Multi-head attention concatenates the outputs of the  $h$  attention heads and applies a linear transformation, enabling the model to attend to different representation subspaces in parallel.

Each attention block is followed by a position-wise feed-forward network, implemented as

$$\text{FFN}(x) = \text{ReLU}(xW_1 + b_1)W_2 + b_2, \quad (14)$$

where  $W_1, W_2$  are learnable weight matrices,  $b_1$  and  $b_2$  are biases, and ReLU introduces non-linearity. Residual connections and layer normalization are applied after both the attention and feed-forward sublayers, ensuring stable gradient propagation. A dropout rate of 0.1 is applied throughout to improve generalization.

At the output of the encoder stage, the encoded trend and residual representations are concatenated and passed through a projection head to produce forecasts for the 48-step horizon. This fusion ensures that both long-term dependencies captured in the trend and localized variations preserved in the residual are exploited in the final prediction. An illustration of the network architecture is shown in Fig. 6.

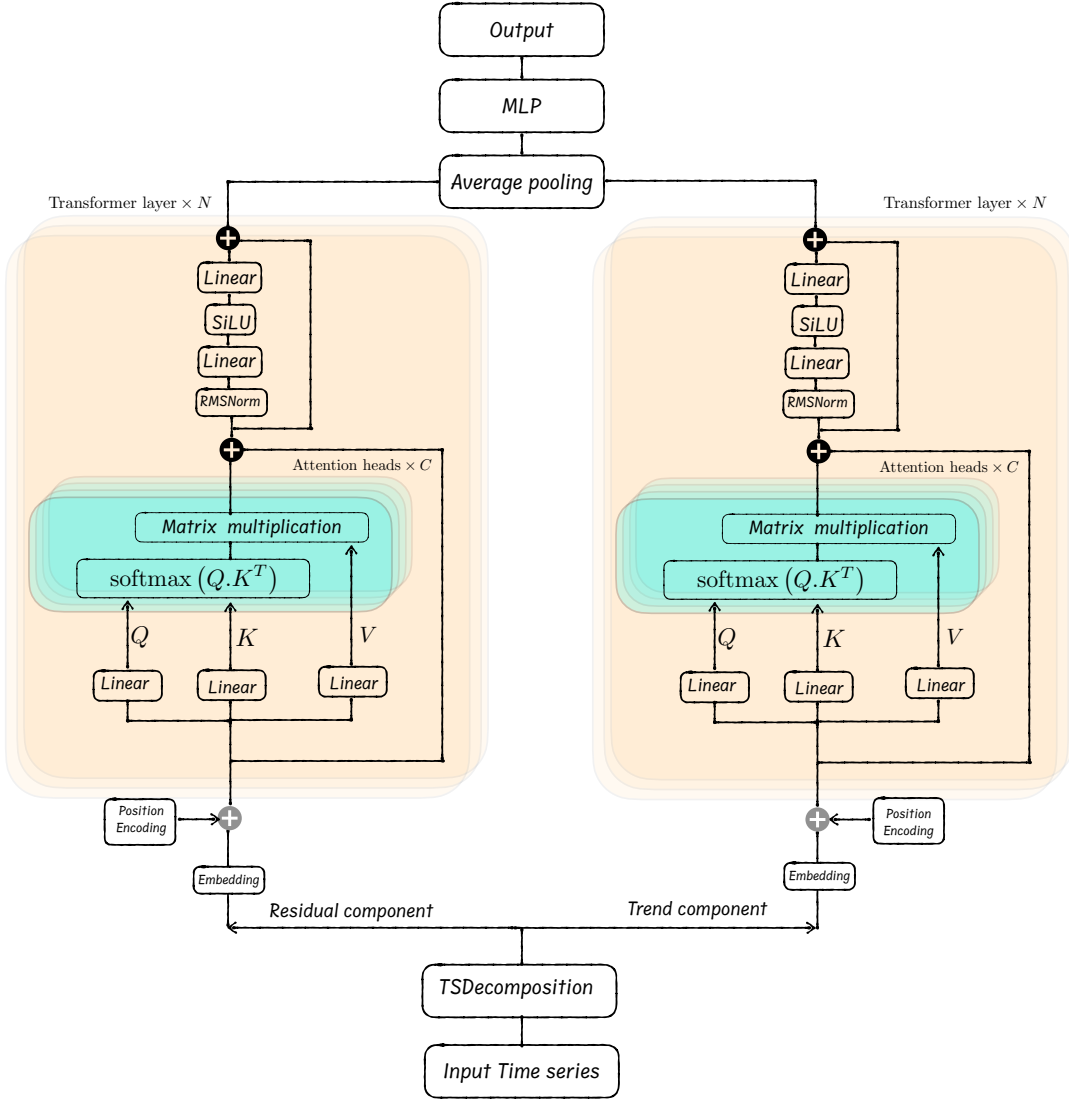


**Figure 6.** Schematic illustration of the used transformer network architecture.

#### 5.3.4. Training

Training is performed end-to-end using the PyTorch Lightning framework. The model is trained with mini-batches of 64 sequences, and 10% of the dataset is held out for validation. The objective is to minimize the mean squared error (MSE) between the predicted horizon and the ground-truth sequence. Optimization is carried out using the Adam algorithm with an initial learning rate of  $5 \times 10^{-6}$ . To enhance convergence stability, a step learning rate scheduler decays the learning rate by a factor of 0.9 every 20 epochs. Training proceeds for up to 100 epochs, although an early stopping criterion with patience of five epochs halts training if no improvement in validation loss is observed. Model checkpoints are saved based on the lowest validation loss, ensuring that the best-performing parameters are retained for evaluation and deployment.

The future behavior of the six sources in our sample, as predicted by both the Transformer and STLForecaster methods, is shown in the light blue highlighted region of Fig. 7.

We start by comparing the predictions on the test set, represented by the pink highlighted region. The Mean Absolute Percentage Error results for the demonstrate the general superiority of the deep learning Transformer method over the

statistical STLForecaster method in learning the complexity of the LC and accurately predicting the sources' behavior. This is particularly apparent in the cases of PKS 1553+113, S5 1044+71 and PKS 0139-09. Qualitatively, in the case of PG 1553+113, the Transformer successfully captured the long-term trend, whereas the LOESS method overestimates it; in the case of S5 1044+71, the detail of the peak at about 6000 MJD is somewhat counterintuitively captured, as one may have expected a naive continuation of the previous pattern apparent by simple inspection of the training set to lead to the broader peaked behavior that is indeed predicted by LOESS; the details of the peaks in the test set are similarly much better represented by the STLForecaster in the case of PKS 0139-09.

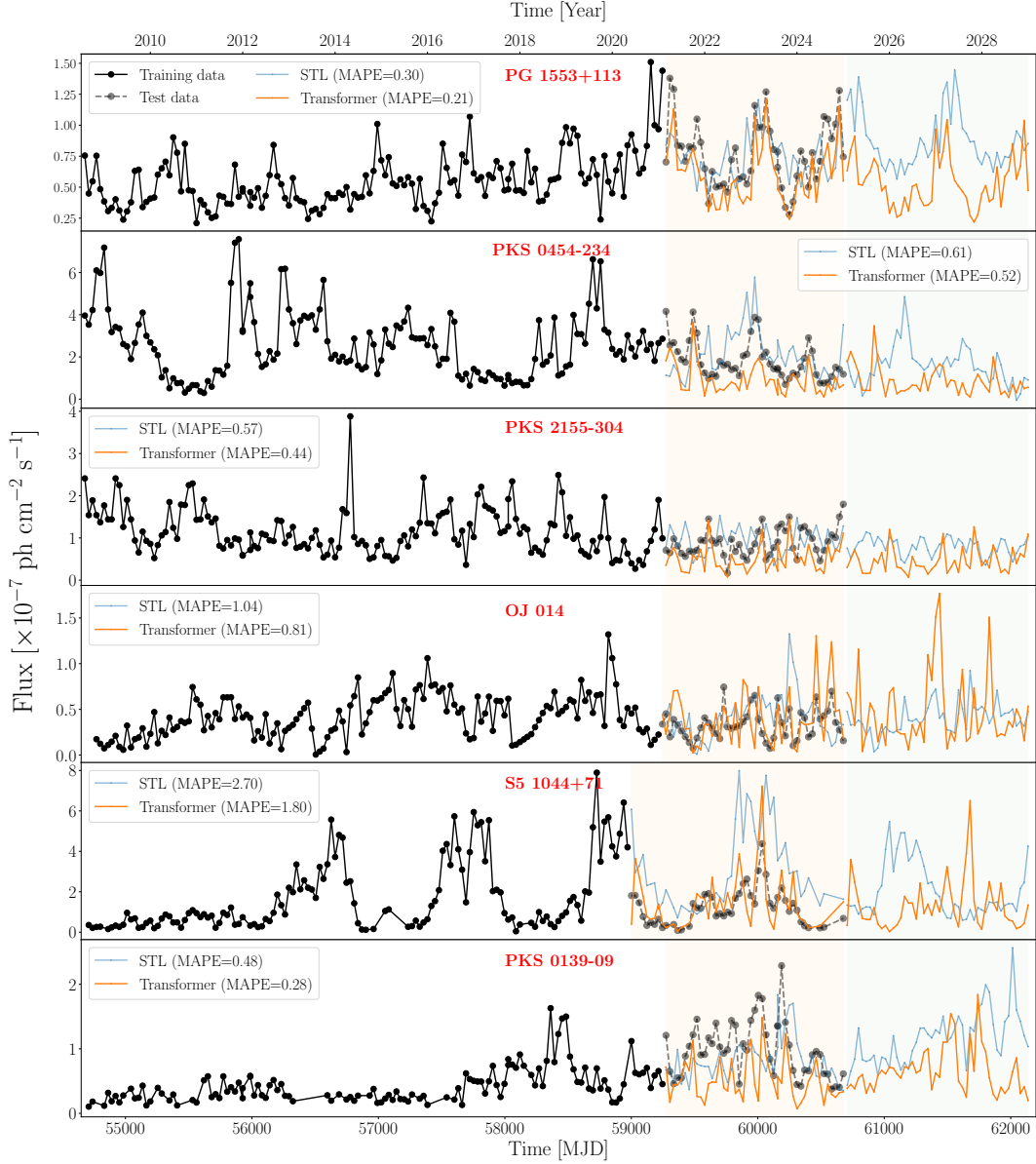


**Figure 7.** Current observed monthly  $\gamma$ -ray light curves and their forecasting for the following four years. The blue and yellow lines represent the light curve predictions on the test set (pink highlighted region) and the future epoch (light blue highlighted region) using STLForecaster and Transformer, respectively. The Mean Absolute Percentage Error (MAPE) for the test set predictions is presented for both methods, the Transformer and the STLForecaster. The prediction on the future epoch is based on the training on the entire observed light curve.

### 5.3.5. Forecast and predictions

Given the encouraging results on the test set, we make predictions regarding future behavior. In general, the Transformer predictions include a weaker future trend. For PG 1553+113, for instance, the QPO cycle starting around 2020 is expected to repeat without further enhancement of the mean signal. A similar conclusion can be made regarding PKS 0454-234, with cycle starting from 2023. In the case of PKS 2155-304, the initial transient high amplitude periodicities (that could be identified on the WWZ diagram in Fig. 2), are expected to completely disappear, with the smaller amplitude oscillations persisting. In the case of OJ 014, on the other hand, large flaring that appears to embody a stochastic component is predicted. For S5 1044+71, the aforementioned unexpected single peak, previously predicted for the test set, is expected to repeat. A similar expectation is predicted for PKS 0139-09, with the double peak starting at  $\gtrsim 6000$  MJD repeating.

The expected future periods and their significances from the application of the LSP method are summarized in Table 4, for both original and detrended  $\gamma$ -ray future LCs of the six blazars considered, where ‘future’ refers to the observed LC plus future data as predicted by the Transformer technique.

The periods of the inferred QPOs are compatible with the observed LCs. Without detrending we find only two cases where QPO signal’s significance increases: the case of PG 1553+113, where the QPO signal appears exceptionally strong and is predicted to persist with high significance; and the new source studied here (PKS 0139-09), where the tentative nascent QPO is expected to strengthen significantly. The future behavior of the LC of this latter source, in particular, will represent a definite test case for the existence and predictability of QPO.

As with the case of the observed light curves, detrending the extended LCs generally enhances the statistical significance of the periods. In particular, the two cases just mentioned (PG 1553+113 and PKS 0139-09), the significance of the QPO increased from  $3.5\sigma$  and  $1.6\sigma$  in the original LC to  $>4.8\sigma$  and  $3.2\sigma$ , respectively, in the detrended and predicted LC.

The general features of our predictions can be outlined as follows. In the case of PG 1553+113, we expect persistent, strong QPO to continue. For cases that showed early transient behavior, namely PKS 0454-234 and PKS 2155-304, a suppressed QPO signal is expected to persist for the extrapolated light curve. On the other hand, we predict significant suppression of the QPO signal, relative to that inferred from the observational data alone, in cases where transience appeared near the end of the period covered by the observational data (OJ 014 and S5 1044+71). Finally, our results suggest significant strengthening of the QPO signal in significance in the case where a nascent QPO signal is apparent (PKS 0139-09).

**Table 4.** Summary of periods and significances inferred from observed and projected data, using the LSP, for both original and detrended light curves.

Source Name	Present Period (yr)		Future Period (yr)	
	Original LC	Detrended LC	Original LC	Detrended LC
PG 1553+113	$2.1_{3.6\sigma}^{\pm 0.13}$	$2.1_{4.5\sigma}^{\pm 0.12}$	$2.1_{4.2\sigma}^{\pm 0.12}$	$2.1_{>4.8\sigma}^{\pm 0.11}$
PKS 0454–234	$3.5_{2.5\sigma}^{\pm 0.35}$	$3.6_{2.6\sigma}^{\pm 0.4}$	$3.6_{2.3\sigma}^{\pm 0.34}$	$3.6_{2.9\sigma}^{\pm 0.73}$
PKS 2155–304	$1.7_{2.6\sigma}^{\pm 0.13}$	$1.7_{3.3\sigma}^{\pm 0.13}$	$1.7_{2.7\sigma}^{\pm 0.18}$	$1.7_{3.4\sigma}^{\pm 0.18}$
OJ 014	$4.2_{3.5\sigma}^{\pm 0.57}$	$4.2_{4.2\sigma}^{\pm 0.53}$	$4.1_{2.9\sigma}^{\pm 0.38}$	$4.0_{2.9\sigma}^{\pm 0.39}$
S5 1044+71	$3.1_{4.4\sigma}^{\pm 0.34}$	$3.1_{4.3\sigma}^{\pm 0.37}$	$3.2_{3.3\sigma}^{\pm 0.53}$	$3.2_{3.6\sigma}^{\pm 0.47}$
PKS 0139–09	$5.2_{1.6\sigma}^{\pm 0.73}$	$5.1_{2.0\sigma}^{\pm 0.96}$	$4.9_{2.0\sigma}^{\pm 0.75}$	$5.0_{3.2\sigma}^{\pm 0.81}$

For more specific predictions, in the two cases where the QPO signal is expected to increase in significance—namely, PG 1553+113 and PKS 0139-09—we expect the upcoming periodic flaring to occur in April 2027 for PG 1553+113 and twin peaks in May and December 2027 in the case of PKS 0139-09. In the two cases where transience was detected near the end of the observational period—namely, OJ 014 and S5 1044+71—we expect the novel behavior to lead to flaring in February 2027 and March 2028 in the case of OJ 014 and in October 2027 in the case of S5 1044+71. The two remaining cases are expected to remain relatively quiescent, with smaller peaks at timescales consistent with the inferred periods.

## 6. CONCLUSION

We conducted a comprehensive temporal analysis of the  $\gamma$ -ray light curves of five blazars that were previously reported to exhibit high-significance ( $>3\sigma$ ) quasiperiodic oscillations on year-long timescales. We extended previous analyses with further data (up to February 2025), examining the persistence of the QPO signals, the existence of long term trends, and their effect on the strengths of the signals. We furthermore forecast the light curves into the future, enabling predictions that may be tested against future data. The above procedures were also applied to one new candidate, the BL Lac PKS 0139-09, where nascent QPOs may be appearing.

To search for periodicities, we initially employed the Lomb-Scargle periodogram (Section 3.1). The inferred periods are consistent with, or within the uncertainties of those previously reported in the literature. However, in general, results for our extended timespan do not show a significant increase in the QPO signal’s strength, but more often the reverse. The clear exception being the case of S5 1044+71, where we find a QPO significance of  $4.4\sigma$ , which is larger than the value  $3.6\sigma$  previously found by Wang et al. (2022).

The general lack of consolidation of QPO signal confidences may be due to the effect of long term trends in the data, which may themselves reflect longer term periodicities, or due to intrinsic transience in the principal QPO signal. We studied both effects; by detrending through an STL decomposition (Section 4.1), and by using the WWZ wavelet technique to look for transients (Section 3.2).

Long term trends are associated with significant red noise, which can suppress the detectability of the principal periodic signals. A key aspect of our analysis addressed its confounding effects, with the central finding being that detrending can in some cases significantly improve the significance of the principal QPO periods (Table 3). The exceptions to this were the sources S5 1044+71, where the low frequency signal associated with the trend is very small compared to the principal peak; and PKS 0454-234, where the lower frequency peak is close to the principal peak (Fig. 2). A notably remarkable feature of this latter case is the repetition of this double peaked structure at smaller periods, some of which are consistent with being harmonics of the principal period. These peaks are ‘secondary’ in the sense that they are of smaller height. But they can, in fact, come with higher significance, as they correspond to more oscillatory cycles. Significant secondary peaks are also present in other cases (PG 1553+113, PKS 2155-304, and PKS 0139-09). A first harmonic has recently been confirmed in the case of PKS J1309+1154 by Readhead et al. (2026).

If harmonic peaks may indeed be detected by analyzing LCs, it seems possible that the principal peaks themselves, which are usually associated with the characteristic times of the physical process leading to the QPO, are in reality harmonics of a longer principal period. The long-term modulations represented by the inferred trends suggest that larger periods may indeed be present. The presence of significant harmonics (or near harmonics) may contribute to an elevated seasonal component in the STL decomposition in some of the light curves (Fig. 3), even when the primary peak significance is relatively weak.

In a couple of cases (PKS 0454-234 and PKS 2155-304), even with detrending the QPO signal significances are markedly lower than found in previous studies. In these cases, clear transients are present in the data early on in the observing period. Indeed, examination of the WWZ diagrams reveals clear transient behavior even for the detrended data; with significant weakening found well within the observed timespan, on a timescale of  $\lesssim 4000$  days for PKS 0454-234, and within  $\sim 3000$  days for PKS 2155-304 (Fig. 4).

In fact, except for PG 1553+113, which displays a persistently strong QPO signal, all sources considered here show transient behavior on a timescale  $\lesssim 4000$  days. While transience in the two sources discussed above results in the suppression of the QPO signal well within the observed timescale, in two other cases (OJ 014 and S5 1044+71), the signal is attenuated near the end of that timespan. In the case S5 1044+71 the QPO signal appears weaker not only near the end of the observational period but also at its start. A weak start is also apparent in the case of the new source, PKS 0139-09. But here the significance of the QPO steadily increases within the whole observational period. In this case, one may thus expect the peak associated with the  $\lesssim 4000$  day QPO mean life to appear in the coming years. To make such statements more precise, and make testable predictions, we introduced future state forecasting.

We used a statistical model, the STLForecaster, as well as a deep learning Transformer architecture, to project the blazars’ data four years into the future (Section 5). Applying the methods on a test set we find that the Transformer outperformed the statistical STLForecaster in prediction accuracy. It is successful in capturing complex, non-linear long-term trends; as evidenced, for example, by its successful prediction of a trend saturation in PG 1553+113, contrary

to the recent historical ( $\approx 10$  yr) upward trend, as well as unexpected flaring in the cases of S5 1044+71 and PKS 0139-09 (Fig. 5). Table 4 lists the values and expected significance of the principal periods.

Sustained oscillations are predicted to continue in the future in the case of PG 1553+113. Indeed, here the significance of the 2.1 year period increased from  $3.6\sigma$  in the original light curve to  $>4.8\sigma$ , when the data was forecast into the future and then detrended. Also, the principal candidate signal in the new BL Lac object PKS 0139-09, which was only marginally detectable ( $1.6\sigma$ ) in the original data showed its significance rise to  $3.2\sigma$  in the detrended extrapolated curve. Thus, a solid testable prediction for this new source is the strengthening of the nascent QPO signal in the coming years.

On the other hand, for the cases where the QPO signal was significantly attenuated near the end of the observed data timescale—namely, in the cases of OJ 014 and S5 1044+71—the late-time suppression is expected to persist. This is reflected in the smaller significance of the QPOs in the time-extrapolated light curves compared to the originals. The persistence of late time behavior is also expected for the cases where the QPO signal significantly died down well within the observed timespan (PKS 0454-234 and PKS 2155-304). As the transient behavior here occurs early on, the expectation is for the QPO significance to remain at a similar level in the extrapolated curves. This reflects the prediction of a new quasi-stationary state that persists through the extrapolation period.

In addition to these generic expected trends, we make specific predictions regarding the future behavior, particularly regarding the dates of upcoming flarings, in the light curves of the objects studied here. These can potentially guide future observations and data analyses, against which they may be tested.

Our inferences and predictions regarding the persistence of year-long periodic signals have implications for their theoretical interpretations. While no single widely accepted theory yet exists to describe the physical mechanisms that may be responsible for QPOs in blazars, a variety of models have been proposed to account for apparent year-long periodicities detected in the data (e.g., Abdollahi et al. 2024 Section 4.1, for a recent summary). These may differ especially in terms of the longer term trends and transient behavior studied here. For example, as mentioned in the introduction, ballistic blobs in the curved jet model should lead to transient decaying signals. On the other hand, purely geometric models invoking jet precession in a binary on a circular orbit (e.g. Sobacchi et al. 2017) may not account for the transient behavior inferred in this study. Likewise with purely rigid precession of a jet driven by torques (Katz 1997) or direct modulation of the accretion flow rate on the SMBH due to torques from a companion, as originally proposed by Sillanpaa et al. (1988). Nevertheless, as they show, the inclusion of a disk potential leads to orbital precession that can be associated with longer term modulations, possibly compatible with the more complex patterns displayed by most systems considered here. Nontrivial time dependence may also ensue from tidal interactions between SMBH disks. Additional flaring, with possible signature signals in specific wavelengths, can result from passage of an SMBH through the accretion disks of the other (Valtaoja et al. 2000). Double jetted models with interactions between the jets may furthermore lead to double peaked periodic patterns (Villata et al. 1998). In addition to simple precession, perturbations of the jet in an SMBHB can lead to furthermore instigate complex magnetohydrodynamic processes (Cavaliere et al. 2017; Nolting et al. 2023). Such precession and associated QPOs may be present even in the absence of a secondary SMBH, notably through Lense-Thirring precession of tilted accretion disks (Bardeen & Petterson 1975; Fragile et al. 2007).

Thus, except possibly for the case of PG 1553+113, the simplest geometric models appear ruled out as sources of QPO by our analysis of the past light curves and predictions for the next years. The time dependencies inferred in this study favor richer scenarios, where further physical processes are triggered (by the presence of a companion SMBH or otherwise). Detailed simulations coupled with Multi-wavelength observations may serve to distinguish between such scenarios. Integrating multi-frequency observations will also help increase the accuracy of the neural network in forecasting future behavior.

#### ACKNOWLEDGEMENTS

The authors thanks Waleed Esmail for the fruitful discussion about the DL analysis. AH is funded by grant number 22H05113, “Foundation of Machine Learning Physics”, Grant in Aid for Transformative Research Areas and 22K03626, Grant-in-Aid for Scientific Research (C). AH is partially supported by the Science, Technology and Innovation Funding Authority (STDF) under grant number 50806.

## SOFTWARE

Fermitools-conda, DELCgen-Simulating light curves (Connolly 2015), NumPy (Harris et al. 2020), SciPy (Virtanen et al. 2020), Matplotlib (Hunter 2007), sktime (Löning et al. 2019), PyTorch (Paszke et al. 2017), REDFIT (Schulz & Mudelsee 2002), astroML (Ivezić et al. 2014). For the purpose of open science, all code and analysis pipelines are available from a public [GitHub repository](#).

## REFERENCES

- Abdollahi, S., Acero, F., Baldini, L., et al. 2022, *The Astrophysical Journal Supplement Series*, 260, 53, doi: 10.3847/1538-4365/ac6751
- Abdollahi, S., Baldini, L., Barbiellini, G., et al. 2024, *The Astrophysical Journal*, 976, 203
- Abhir, J., Joseph, J., Patel, S. R., & Bose, D. 2021, *Monthly Notices of the Royal Astronomical Society*, 501, 2504. <https://doi.org/10.1093/mnras/staa3639>
- Ackermann, M., Ajello, M., Albert, A., et al. 2015, *ApJL*, 813, L41, doi: 10.1088/2041-8205/813/2/L41
- Ackermann, M., Ajello, M., Albert, A., et al. 2015, *The Astrophysical Journal Letters*, 813, L41
- Agarwal, A., Mihov, B., Andruchow, I., et al. 2021, *A&A*, 645, A137, doi: 10.1051/0004-6361/202039301
- Agazie, G., Anumalapudi, A., Archibald, A. M., et al. 2023, *ApJL*, 951, L50, doi: 10.3847/2041-8213/ace18a
- Atwood, W., Abdo, A. A., Ackermann, M., et al. 2009, *The Astrophysical Journal*, 697, 1071
- Atwood, W., Albert, A., Baldini, L., et al. 2013, arXiv e-prints, arXiv:1303.3514, doi: 10.48550/arXiv.1303.3514
- Bardeen, J. M., & Petterson, J. A. 1975, *ApJL*, 195, L65, doi: 10.1086/181711
- Begelman, M. C., Blandford, R. D., & Rees, M. J. 1980, *Nature*, 287, 307. <https://doi.org/10.1038/287307a0>
- Benkhali, F. A., Hofmann, W., Rieger, F., & Chakraborty, N. 2020, *Astronomy & Astrophysics*, 634, A120. <https://doi.org/10.1051/0004-6361/201935117>
- Bhatta, G., & Dhital, N. 2020, *The Astrophysical Journal*, 891, 120. <https://doi.org/10.3847/1538-4357/ab7455>
- Blandford, R., Meier, D., & Readhead, A. 2019, *Annual Review of Astronomy and Astrophysics*, 57, 467. <https://doi.org/10.1146/annurev-astro-081817-051948>
- Cavaliere, A., Tavani, M., & Vittorini, V. 2017, *ApJ*, 836, 220, doi: 10.3847/1538-4357/836/2/220
- Chen, Y., Yi, T., Chen, J., et al. 2024, *NewA*, 108, 102186, doi: 10.1016/j.newast.2023.102186
- Chevalier, J., Sanchez, D. A., Serpico, P. D., Lenain, J.-P., & Maurin, G. 2019, *MNRAS*, 484, 749, doi: 10.1093/mnras/stz027
- Cleveland, B. 1990, *J Off Stat*, 6, 3
- Colpi, M., Danzmann, K., Hewitson, M., et al. 2024, arXiv e-prints, arXiv:2402.07571, doi: 10.48550/arXiv.2402.07571
- Connolly, S. 2015, arXiv e-prints, arXiv: 1503.06676
- de la Parra, P. V., Kiehlmann, S., Mróz, P., et al. 2025, *ApJ*, 987, 191, doi: 10.3847/1538-4357/addc60
- D’Orazio, D. J., & Charisi, M. 2023, arXiv e-prints, arXiv:2310.16896, doi: 10.48550/arXiv.2310.16896
- Doğan, S., Nixon, C., King, A., & Price, D. J. 2015, *MNRAS*, 449, 1251, doi: 10.1093/mnras/stv347
- Emmanoulopoulos, D., McHardy, I., & Papadakis, I. 2013, *Monthly Notices of the Royal Astronomical Society*, 433, 907. <https://doi.org/10.1093/mnras/stt764>
- Farris, B. D., Duffell, P., MacFadyen, A. I., & Haiman, Z. 2014, *ApJ*, 783, 134, doi: 10.1088/0004-637X/783/2/134
- Foster, G. 1996, *The Astronomical Journal*, 112, 1709. <https://doi.org/10.1086/118137>
- Fragile, P. C., Blaes, O. M., Anninos, P., & Salmonson, J. D. 2007, *ApJ*, 668, 417, doi: 10.1086/521092
- Goyal, A. 2018, *Galaxies*, 6, 34, doi: 10.3390/galaxies6010034
- Goyal, A., Stawarz, L., Ostrowski, M., et al. 2017, *The Astrophysical Journal*, 837, 127, doi: 10.3847/1538-4357/aa6000
- Hammad, A., Moretti, S., & Nojiri, M. 2024, *JHEP*, 03, 144, doi: 10.1007/JHEP03(2024)144
- Hammad, A., & Nojiri, M. M. 2024, *JHEP*, 06, 176, doi: 10.1007/JHEP06(2024)176
- Harris, C. R., Millman, K. J., Van Der Walt, S. J., et al. 2020, *Nature*, 585, 357
- Hashad, M., EL-Zant, A. A., & Abdou, Y. 2023, *Advances in Space Research*, 72, 3538. <https://doi.org/10.1016/j.asr.2023.06.042>
- Hashad, M. A., EL-Zant, A. A., Abdou, Y., & Badran, H. M. 2024, *ApJ*, 975, 164, doi: 10.3847/1538-4357/ad7a6e
- Hunter, J. D. 2007, *Computing in science & engineering*, 9, 90. <https://doi.org/10.1109/MCSE.2007.55>
- Hyndman, R. J., & Athanasopoulos, G. 2021, *Forecasting: principles and practice*, 3rd edition (OTexts: Melbourne, Australia.). [OTexts.com/fpp3](https://www.otexts.com/fpp3)

- Ivezić, z., Connolly, A. J., VanderPlas, J. T., & Gray, A. 2014, *Statistics, data mining, and machine learning in astronomy* (Princeton University Press). <https://doi.org/10.23943/princeton/9780691151687.001.0001>
- Katz, J. I. 1997, *ApJ*, 478, 527, doi: 10.1086/303811
- Kiehlmann, S., de la Parra, P. V., Sullivan, A. G., et al. 2025a, *ApJ*, 985, 59, doi: 10.3847/1538-4357/adc567
- . 2025b, *ApJ*, 985, 59, doi: 10.3847/1538-4357/adc567
- Krause, M. G. H., Bourne, M. A., Britzen, S., et al. 2025, *PASA*, 42, e162, doi: 10.1017/pasa.2025.10120
- Lomb, N. R. 1976, *Astrophysics and space science*, 39, 447. <https://doi.org/10.1007/BF00648343>
- Löning, M., Bagnall, A., Ganesh, S., et al. 2019, arXiv e-prints, arXiv:1909.07872, doi: 10.48550/arXiv.1909.07872
- Madejski, G. G., & Sikora, M. 2016, *Annual Review of Astronomy and Astrophysics*, 54, 725–760, doi: 10.1146/annurev-astro-081913-040044
- Maiolino, R., Scholtz, J., Curtis-Lake, E., et al. 2024, *A&A*, 691, A145, doi: 10.1051/0004-6361/202347640
- Makridakis, S., Wheelwright, S. C., & Hyndman, R. J. 1998, *Forecasting Methods and Applications*, 3rd edn. (New York: John Wiley & Sons)
- Mohan, P., & Mangalam, A. 2015, *The Astrophysical Journal*, 805, 91. <https://doi.org/10.1088/0004-637X/805/2/91>
- Molina, B., Mróz, P., De la Parra, P. V., et al. 2025, arXiv e-prints, arXiv:2510.23103, doi: 10.48550/arXiv.2510.23103
- Nolting, C., Ball, J., & Nguyen, T. M. 2023, *ApJ*, 948, 25, doi: 10.3847/1538-4357/acc652
- Paszke, A., Gross, S., Chintala, S., et al. 2017, in *NIPS Workshop*
- Peñil, P., Ajello, M., Buson, S., et al. 2025, *MNRAS*, 541, 2955, doi: 10.1093/mnras/staf1108
- Peñil, P., Otero-Santos, J., Banerjee, A., et al. 2025a, *Astronomy & Astrophysics*, 700, A208, doi: 10.1051/0004-6361/202555599
- . 2025b, *Astronomy & Astrophysics*, 700, A208, doi: 10.1051/0004-6361/202555599
- Peñil, P., Domínguez, A., Buson, S., et al. 2020, *The Astrophysical Journal*, 896, 134. <https://doi.org/10.3847/1538-4357/ab910d>
- Peñil, P., Otero-Santos, J., Ajello, M., et al. 2024, *Monthly Notices of the Royal Astronomical Society*, 529, 1365–1385, doi: 10.1093/mnras/stae594
- Pfeifle, R. W., Weaver, K. A., Secrest, N. J., Rothberg, B., & Patton, D. R. 2025, *ApJS*, 281, 25, doi: 10.3847/1538-4365/adf845
- Press, W. H. 1978, *Comments on Astrophysics*, 7, 103
- Prokhorov, D., & Moraghan, A. 2017, *Monthly Notices of the Royal Astronomical Society*, 471, 3036. <https://doi.org/10.1093/mnras/stx1742>
- Puerto-Sánchez, C., Habouzit, M., Volonteri, M., et al. 2025, *MNRAS*, 536, 3016, doi: 10.1093/mnras/stae2763
- Readhead, A. C. S., Aller, M. F., Sullivan, A. G., et al. 2026, *ApJL*, 996, L39, doi: 10.3847/2041-8213/ae2656
- Ren, H. X., Cerruti, M., & Sahakyan, N. 2023, *Astronomy & Astrophysics*, 672, A86, doi: 10.1051/0004-6361/202244754
- Rico, A., Domínguez, A., Peñil, P., et al. 2025, *A&A*, 697, A35, doi: 10.1051/0004-6361/202452495
- Rieger, F. M. 2004, *The Astrophysical Journal*, 615, L5. <https://doi.org/10.1086/426018>
- . 2019, *Galaxies*, 7, 28. <https://doi.org/10.3390/galaxies701002>
- Rueda, H., Glicenstein, J.-F., & Brun, F. 2022, *ApJ*, 934, 6, doi: 10.3847/1538-4357/ac771c
- Sandrinelli, A., Covino, S., & Treves, A. 2014, *ApJL*, 793, L1, doi: 10.1088/2041-8205/793/1/L1
- Sarkar, A., Gupta, A. C., Chitnis, V. R., & Wiita, P. J. 2021, *Monthly Notices of the Royal Astronomical Society*, 501, 50–61, doi: 10.1093/mnras/staa3211
- Scargle, J. D. 1982, *The Astrophysical Journal*, 263, 835. <https://doi.org/10.1086/160554>
- Schulz, M., & Mudelsee, M. 2002, *Computers & Geosciences*, 28, 421. [https://doi.org/10.1016/S0098-3004\(01\)00044-9](https://doi.org/10.1016/S0098-3004(01)00044-9)
- Sharma, A., Banerjee, A., Das, A. K., Mandal, A., & Bose, D. 2024, *ApJ*, 975, 56, doi: 10.3847/1538-4357/ad7391
- Shin, D., & Zhang, E. 2025, arXiv preprint arXiv:2505.12761
- Sillanpaa, A., Haarala, S., Valtonen, M. J., Sundelius, B., & Byrd, G. G. 1988, *ApJ*, 325, 628, doi: 10.1086/166033
- Sobacchi, E., Sormani, M. C., & Stamerra, A. 2017, *MNRAS*, 465, 161, doi: 10.1093/mnras/stw2684
- Stellingwerf, R. F. 1978, *ApJ*, 224, 953, doi: 10.1086/156444
- Tantry, J., Sharma, A., Shah, Z., Iqbal, N., & Bose, D. 2025, *Journal of High Energy Astrophysics*, 47, 100372, doi: 10.1016/j.jheap.2025.100372
- Tarnopolski, M., Żywucka, N., Marchenko, V., & Pascual-Granado, J. 2020, *The Astrophysical Journal Supplement Series*, 250, 1, doi: 10.3847/1538-4365/aba2c7
- Tavani, M., Cavaliere, A., Munar-Adrover, P., & Argan, A. 2018, *The Astrophysical Journal*, 854, 11. <https://doi.org/10.3847/1538-4357/aaa3f4>

- Torrence, C., & Compo, G. P. 1998, *Bulletin of the American Meteorological Society*, 79, 61, doi: 10.1175/1520-0477(1998)079<0061:APGTWA>2.0.CO;2
- Ulrich, M.-H., Maraschi, L., & Urry, C. M. 1997, *Annual Review of Astronomy and Astrophysics*, 35, 445–502, doi: 10.1146/annurev.astro.35.1.445
- Urry, C. M., & Padovani, P. 1995, *Publications of the Astronomical Society of the Pacific*, 107, 803. <https://doi.org/10.1086/133630>
- Urry, M. 2011, *Journal of Astrophysics and Astronomy*, 32, 139–145, doi: 10.1007/s12036-011-9072-x
- Valtaoja, E., Teräsanta, H., Tornikoski, M., et al. 2000, *ApJ*, 531, 744, doi: 10.1086/308494
- VanderPlas, J. T. 2018, *The Astrophysical Journal Supplement Series*, 236, 16. <https://doi.org/10.3847/1538-4365/aab766>
- Vaswani, A., Shazeer, N., Parmar, N., et al. 2017, *Advances in neural information processing systems*, 30
- Vaughan, S., Uttley, P., Markowitz, A., et al. 2016, *Monthly Notices of the Royal Astronomical Society*, 461, 3145. <https://doi.org/10.1093/mnras/stw1412>
- Villata, M., Raiteri, C. M., Sillanpaa, A., & Takalo, L. O. 1998, *MNRAS*, 293, L13, doi: 10.1046/j.1365-8711.1998.01244.x
- Virtanen, P., Gommers, R., Oliphant, T. E., et al. 2020, *Nature Medicine*, 17, 261, doi: 10.1038/s41592-019-0686-2
- Volonteri, M., Haardt, F., & Madau, P. 2003, *ApJ*, 582, 559, doi: 10.1086/344675
- Wang, G., Cai, J., & Fan, J. 2022, *The Astrophysical Journal*, 929, 130. <https://doi.org/10.3847/1538-4357/ac5b08>
- Wang, X., Smith, K., & Hyndman, R. 2006, *Data Mining and Knowledge Discovery*, 13, 335–364, doi: 10.1007/s10618-005-0039-x
- Welsh, W. F. 1999, *PASP*, 111, 1347, doi: 10.1086/316457
- Wen, Q., Zhou, T., Zhang, C., et al. 2022, arXiv preprint arXiv:2202.07125
- Wood, M., Caputo, R., Charles, E., et al. 2017, in *Proceedings of 35th International Cosmic Ray Conference — PoS(ICRC2017)*, ICRC2017 (Sissa Medialab), doi: 10.22323/1.301.0824
- Zechmeister, M., & Kürster, M. 2009, *Astronomy & Astrophysics*, 496, 577. <https://doi.org/10.1051/0004-6361/200811296>
- Zhang, P.-f., Yan, D.-h., Liao, N.-h., & Wang, J.-c. 2017, *ApJ*, 835, 260, doi: 10.3847/1538-4357/835/2/260